JAMES | Journal of Advances in Modeling Earth Systems

RESEARCH ARTICLE
10.1029/2020MS002086

Response of Tropical Cyclone Formation and Intensification Rates to Climate Warming in Idealized Simulations

Hamish A. Ramsay[1], **Martin S. Singh**[2], **and Daniel R. Chavas**[3]

[1]CSIRO Oceans and Atmosphere, Aspendale, Victoria, Australia, [2]School of Earth, Atmosphere and Environment, Monash University, Clayton, Victoria, Australia, [3]Department of Earth, Atmospheric, and Planetary Sciences, Purdue University, West Lafayette, IN, USA

Key Points:

- Tropical cyclones (TCs) develop spontaneously in rotating radiative-convective equilibrium, even in the absence of interactive radiation
- The time taken for a TC to develop from a quiescent initial state exhibits a distinctive nonmonotonic dependence on surface warming
- TC intensification rate increases strongly with warming, with much larger variation than that predicted by extant theory

Correspondence to:
H. A. Ramsay,
hamish.ramsay@csiro.au

Citation:
Ramsay, H. A., Singh, M. S., & Chavas, D. R. (2020). Response of tropical cyclone formation and intensification rates to climate warming in idealized simulations. *Journal of Advances in Modeling Earth Systems*, *12*, e2020MS002086. https://doi.org/10.1029/2020MS002086

Received 24 FEB 2020
Accepted 14 SEP 2020
Accepted article online 17 SEP 2020

Abstract There is currently no theory for the rate of tropical cyclone (TC) formation given a particular climate, so our understanding of the relationship between TC frequency and large-scale environmental factors is largely empirical. Here, we explore the sensitivity of TC formation and intensification rates to climate warming in a series of highly idealized cloud-permitting simulations, in which TCs form spontaneously from a base state of rest on an *f*-plane. The simulations reveal a nonmonotonic relationship between the time taken for a TC precursor disturbance (a "seed") to form and the prescribed sea surface temperature (SST), with moderately long seed emergence times at both ends of the SST range tested (292 and 304 K) and a shorter seed emergence time at the middle value of SST (298 K). Genesis potential indices (GPIs) exhibit a different response to warming: either a monotonic increase if the potential intensity and midtropospheric relative humidity are used or relatively little sensitivity if the saturation deficit is used as the humidity variable. The sensitivity of elapsed time between a TC seed disturbance and TC genesis to surface warming is, however, generally well captured by GPIs, especially those that depend on the saturation deficit. The maximum intensification rate of TCs increases strongly with warming, particularly during the second half of the intensification process. Notably, storms intensify much more rapidly with increasing temperature than is predicted by extant theory based on potential intensity, suggesting that TCs in a warmer climate may intensify even more rapidly than recent studies suggest.

Plain Language Summary Climate change is expected to exacerbate tropical cyclone (TC) hazards, such as extreme rainfall, but there is less certainty in the projections of the overall frequency of TCs as the climate continues to warm. Here, we explore how the formation and intensification of TCs respond to a warmer climate using computer simulations that capture the full evolution of a TC, from a cluster of tropical clouds to a Category 5 hurricane in a controlled environment. Our simulations reveal a complex relationship between the likelihood of TC formation and sea surface temperature that cannot be explained by a simple trend. The maximum intensification rate of TCs, on the other hand, increases strongly with warming, suggesting that rapidly intensifying storms may become more frequent in future climate and intensify faster as the world's oceans continue to warm.

1. Introduction

The global annual rate of tropical cyclone (TC) formation has been remarkably steady since the start of reliable satellite imagery, with a mean of somewhere between 80 and 90 storms per year (Frank & Young, 2007; Lander & Guard, 1998; Maue, 2011; Ramsay, 2017; Schreck et al., 2014). The physical constraints determining this rate are not well understood as there is no extant theory for global TC frequency given a particular climate. Why do roughly 80 TCs develop each year, and why not half or double this number?

Most global climate models (GCMs) simulate a decrease in the frequency of TC-like vortices under future global warming (Christensen et al., 2013; Knutson et al., 2010, 2020; Walsh et al., 2016), particularly in the Southern Hemisphere. But the physical mechanisms of this projected decrease and the implications for future TC frequency remain unclear (Knutson et al., 2020). Moreover, the global oceans have warmed by at least half a degree Celsius since about 1970, yet the global number of storms during this period has remained relatively steady (e.g., Maue, 2011), suggesting that any underlying anthropogenic signal in global TC frequency trends up to this point, if present, may be masked by multidecadal variability

(Sobel et al., 2016). Other possible factors contributing to this apparent discrepancy between historical observations and model projections are discussed in Knutson et al. (2020). There is at least some counterevidence to suggest TC frequency may actually increase in the future. Studies in which the output from GCMs is used to drive statistical or physical models of TCs (Emanuel, 2013, 2020) as well as recent high-resolution GCM projections (e.g., Geophysical Fluid Dynamics Laboratory's (GFDL) HiFLOR model; Bhatia et al., 2018; Vecchi et al., 2019) have found higher frequencies of TCs under 21st-century warming. But it is not yet possible to test these or any other projections given the relatively short reliable historical record (~40 years) compared to the much longer period over which climate change forcings are typically evaluated (~100 years).

A number of alternative approaches have been developed to understand the climate dependence of TC frequency. Two such approaches—genesis potential indices (GPIs) and idealized "TC World" simulations—are discussed briefly below.

1.1. GPIs

It is well known that TCs tend to form in preferred geographical regions of the world (Gray, 1968; Ramsay, 2017; Schreck et al., 2014; Tory et al., 2018); for instance, they rarely form poleward of 30°S in the Southern Hemisphere (40°N in the Northern Hemisphere) or at latitudes very close to the Equator, and there is a near absence of TCs in the eastern South Pacific and South Atlantic basins. Palmen (1948) first proposed a critical sea surface temperature (SST) threshold of about 26.5°C (80°F) for TC genesis and growth, but it is now known that TCs can form below this threshold (e.g., Cione, 2015; Dare & McBride, 2011; Defforge & Merlis, 2017; Tory & Dare, 2015). The notion of an absolute SST threshold has also been challenged on theoretical grounds (e.g., Johnson & Xie, 2010), and a number of studies have simulated TCs over a very broad range of SSTs (e.g., Cronin & Chavas, 2019; Korty et al., 2017), including the Last Glacial Maximum (Korty et al., 2012). In addition to SST dependence, Gray (1968) observed that the climatology of TC formation could be related to several large-scale features of the global circulation, including the Intertropical Convergence Zone (ITCZ), monsoon troughs, instability of the lower troposphere, and vertical shear of the zonal wind between 850 and 200 hPa. Based on these observations, Gray (1979) developed the first GPI, suggesting that "seasonal tropical cyclone frequency can be directly related on a climatological or seasonal basis to a combination of six physical parameters," namely, (i) low-level relative vorticity, (ii) planetary vorticity (f), (iii) vertical wind shear, (iv) SSTs above 26°C, (v) the vertical gradient of θ_e below 500 hPa, and (vi) midtropospheric relative humidity (RH). More recent studies have shown TC genesis to depend on a vorticity "threshold" (e.g., McGauley & Nolan, 2011; Tippett et al., 2011), and the dynamical dependence of genesis rate on the absolute vorticity has also been confirmed in aquaplanet experiments with uniform thermal forcing (Chavas & Reed, 2019). Emanuel and Nolan (2004) reconceptualized Gray's GPI (hereafter, GPI-EN04; see Equation 2) to account for factors that are themselves expected to vary with global climate change (e.g., by replacing SST with potential intensity (PI), symbolized as V_p when expressed in terms of wind speed). Many other genesis indices have been proposed in the literature (e.g., Bruyère et al., 2012; DeMaria et al., 2001; Emanuel, 2010; McGauley & Nolan, 2011; Royer et al., 1998; Tang & Emanuel, 2012; Tippett et al., 2011), and the interested reader is referred to Menkes et al. (2012) for a review.

Although GPIs have been shown to reproduce several aspects of observed global and regional TC variability (e.g., Camargo et al., 2007; Emanuel, 2010; Tippett et al., 2011), when applied to GCM projections they often exhibit an increase with warming (e.g., Camargo, 2013; Camargo et al., 2014; Emanuel, 2013), contrary to the consensus decline in TC frequency based on explicitly simulated TC-like systems in CMIP5 models (Christensen et al., 2013; Knutson et al., 2020). Camargo (2013) showed that GPI-EN04 increases in future climate in most CMIP5 models under the RCP8.5 scenario, while the frequency of simulated TC-like storms had a mixed response to warming with both increases and decreases, depending on the model. Camargo et al. (2014) later demonstrated that a future reduction of TC frequency was reproduced by the GPI of Tippett et al. (2011) when the midlevel RH was replaced with the column saturation deficit. More recently, Lee et al. (2020) found using a statistical-dynamical technique for simulating many thousands of "synthetic" TCs (the Columbia Hazards model (CHAZ); Lee et al., 2018) given gridded climate data that the projected annual frequency of storms was sensitive to the humidity variable used in the GPI component of the model. Specifically, if RH was used, the technique produced an increasing trend of TC frequency, whereas if saturation deficit was used, the technique produced a decreasing trend. Emanuel (2013, 2020), using a different synthetic track model (Emanuel, 2006; Emanuel et al., 2008), found that the global number of synthetic

TCs increased in simulated future climates when forced with environments generated by CMIP5 and CMIP6 models. The seeding technique in the Emanuel model is more or less random and does not depend on GPI trends (unlike the CHAZ model); nevertheless, Emanuel (2013, 2020) found increasing trends in both the global number of synthetic storms and an independently evaluated GPI, even despite the use of saturation deficit in the GPI formulation.

1.2. "TC Worlds" and Spontaneous Tropical Cyclogenesis

The so-called "TC World" simulations provide another approach for investigating the relationship between TCs and climate. In this approach, TCs are simulated within a parameter space that is stripped back from the complexities of the real world, allowing for a more direct evaluation of the relationship between the model's climate (e.g., surface forcing, background rotation rate, vertical wind shear, and radiative forcing) and characteristics of the simulated TCs (e.g., frequency, intensity, and size). These simulations have been performed using a hierarchy of model configurations and forcings, ranging from doubly periodic cloud-resolving models (CRMs) on an *f*-plane to Earth-like aquaplanet GCMs (see Merlis & Held, 2019 for a review).

In doubly periodic *f*-plane CRM simulations, TCs have been shown to form spontaneously (i.e., without a preexisting vortex) under uniform thermal forcing (e.g., Bretherton et al., 2005; Brown & Hakim, 2013; Cronin & Chavas, 2019; Davis, 2015; Khairoutdinov & Emanuel, 2013; Muller & Romps, 2018; Nolan et al., 2007; Wang et al., 2019; Wing et al., 2016). Under Earth-like parameters, computational constraints on the domain size of these simulations typically only allow for a single TC. However, if the size of storms is artificially reduced by increasing *f* by about an order of magnitude, multiple TCs are able to be simulated on domains of order ~1,000 km in width (e.g., Cronin & Chavas, 2019; Khairoutdinov & Emanuel, 2013; Muller & Romps, 2018). Khairoutdinov and Emanuel (2013) used this technique to show that the average number of TCs decreased monotonically with increasing SST (~7% decrease per degree warming) when *f* was set to 2×10^{-4} s^{-1}. However, in these TC worlds, the model domain saturates with TCs, and the total number of very persistent storms is determined by the spacing between them. There is no loss mechanism (e.g., migration over land or strong vertical shear), and storms survive so long as they compete for available moisture (Held & Zhao, 2008). The relevance to observed global TC frequency is therefore unclear.

When a more realistic value of *f* is used, which results in the development of a single TC for practical domain widths of ~1,000–1,500 km, TC frequency is also difficult to define. But the propensity for TC formation may be argued to be related to the speed at which a TC forms, for example, the time it takes for a vortex to reach a specified threshold intensity from a weak initial vortex, referred to as the "incubation period" (e.g., Nolan, 2007; Nolan et al., 2007; Nolan & Rappin, 2008; Rappin et al., 2010). If the incubation period is shorter for one set of large-scale parameters compared to another, then the background environment is arguably more conducive to TC formation and, by extension, to TC frequency. CRMs used in this way can therefore serve as a testbed for evaluating empirically derived GPIs given a particular set of large-scale parameters (e.g., Nolan et al., 2007). And while this approach may not directly tell us about the response of TC genesis to a different climate, the resolved and subgrid-scale processes in the CRM can help determine the mechanisms that might affect genesis under varying conditions.

In this study, we use a CRM to test the dependence of the incubation period and intensification rate on SST over a fairly wide range. We also examine the time taken for a precursor "seed" disturbance to develop from the initial state, building on the previous work noted above. The simulated seed disturbances here are analogous to the weak initial vortices used in previous work on TC incubation and climate (e.g., Nolan et al., 2007; Rappin et al., 2010), except in this study, they evolve from a quiescent initial state with no external noise (e.g., Carstens & Wing, 2020; Davis, 2015; Wing et al., 2016).

The first part of this work explores the emergence time of a TC precursor disturbance (the "time to seed") and its sensitivity to SST (section 3.1), followed by a similar analysis for the incubation period (section 3.2). This behavior is evaluated with respect to changes in GPIs derived from the background state, as well in terms of the evolution of the lower-tropospheric humidity distribution (section 3.3). The second part explores the simulated intensification rate and its dependence on SST (section 4), with comparison to extant theory (Emanuel, 2012). Our findings are discussed in section 5. All simulations are performed on an *f*-plane corresponding to 20°N, with doubly periodic boundaries and a fixed radiative cooling rate. Our approach is conceptually similar to that of Nolan et al. (2007), except here our focus is on the sensitivity of TC

development to variations in SST using a set of mini ensembles, and we additionally consider the time taken for the seed disturbance to form from an initial state of rest. Other differences are discussed in section 2 below.

2. Model Description and Experimental Design

2.1. Model Description

All simulations are performed on the nonhydrostatic Cloud Model 1 (CM1, v19.5) (Bryan, 2003; Bryan & Fritsch, 2002). CM1 has been used extensively to study the behavior of TCs in both axisymmetric and three-dimensional geometry (e.g., Bryan & Rotunno, 2009; Chavas & Emanuel, 2014; Davis, 2015; Hakim, 2011; Kepert et al., 2016; Kilroy & Smith, 2015; Ramsay, 2013; Wang et al., 2019). The model domain is 1,568 km × 1,568 km × 25 km, with a constant horizontal grid spacing of 4 km and a stretched vertical grid with 59 vertical levels that starts at $z = 50$ m (scalars at $z = 25$ m) and smoothly increases to a constant Δz of 500 m above 5 km. The lateral boundary conditions are periodic, and a Rayleigh damping layer is applied to the vertical grid above 20 km to reduce the influence of reflected gravity waves. An adaptive time step is used to speed up integration time. Cloud microphysics are parameterized using the Morrison double-moment scheme (Morrison et al., 2005, 2009). Surface fluxes are calculated using simple bulk aerodynamic formulae but with a constant background surface wind speed of 3 m s^{-1} added to the wind speed used in the calculation of sensible and latent heat fluxes to prevent the free troposphere from becoming excessively cool. The surface drag coefficient C_d is variable, based on Fairall et al. (2003) at low wind speeds (C_d increases from 1.0×10^{-3} at 3 m s^{-1} to 2.3×10^{-3} at 20 m s^{-1}) and Donelan et al. (2004) at high wind speeds (capped at 2.4×10^{-3} for surface winds >25 m s^{-1}). The surface exchange coefficient for enthalpy C_k is fixed at 1.2×10^{-3}, based on measurements of turbulent fluxes in the TC boundary layer from a number of field experiments (Drennan et al., 2007). Heating from frictional dissipation is included. The planetary boundary layer is parametrized using a simple Smagorinsky-like scheme for turbulence, in which the horizontal eddy viscosity depends on a horizontal length scale l_h, which itself is a function of surface pressure ($l_h = 100$ m for SLP of 1,015 hPa and increases linearly to $l_h = 1{,}000$ m for SLP of 900 hPa) (Bryan, 2012). For the simulations investigated here, and depending on SST, the maximum value of l_h varies between 140 and 204 m at the time of precursor TC seed disturbances, 195 and 290 m at TC genesis, and 521 and 1,000 m near the time of peak intensity. The O(1,000 m) length scale for strong hurricanes was determined primarily on the basis of axisymmetric simulations (Bryan, 2012). In situ aircraft observations of turbulent flow in the eyewall region of strong hurricanes suggest an average value of 750 m for l_h, corresponding to a mean wind speed of ~52 m s^{-1}(Zhang & Montgomery, 2012). The 4-km horizontal grid spacing in the three-dimensional simulations here would account for some of the turbulent exchange in the eye-wall region, so the maximum value of l_h should probably be reduced slightly compared to axisymmetric simulations, but determining the optimal value of l_h is beyond the scope of this work. The vertical length scale is a function of height, tending toward ku^*z near the surface, where k is von Kármán's constant and u^* is the friction velocity, and approaching 100 m as $z \to \infty$.

A simple radiative cooling scheme is employed following Ramsay (2013) in which the tropospheric cooling rate is fixed, while the stratospheric temperature is relaxed to a specified value so as to be nearly isothermal. With this setup, the radiative temperature tendency is given by

$$\frac{dT}{dt} = \begin{cases} -1.2 \text{ K day}^{-1}, & \text{for } T > T_{\text{strat}} \\ \dfrac{T_{\text{strat}} - T}{5 \text{ days}}, & \text{elsewhere} \end{cases} \quad (1)$$

where T_{strat} is the stratospheric temperature, set to 198 K. Note that this formulation ignores changes in lower stratospheric temperature that may affect the PI of TCs (e.g., Emanuel et al., 2013; Ramsay, 2013; Vecchi et al., 2013; Wang et al., 2014) and thus GPIs.

2.2. Experimental Design

We conduct a series of five-member ensemble simulations for SSTs ranging from 292 to 304 K in 3 K intervals. Each ensemble member is run for 100 days (or 120 days in the case of one simulation at 304 K in order to sample TC intensification) and initialized from an equilibrated thermodynamic state taken from an

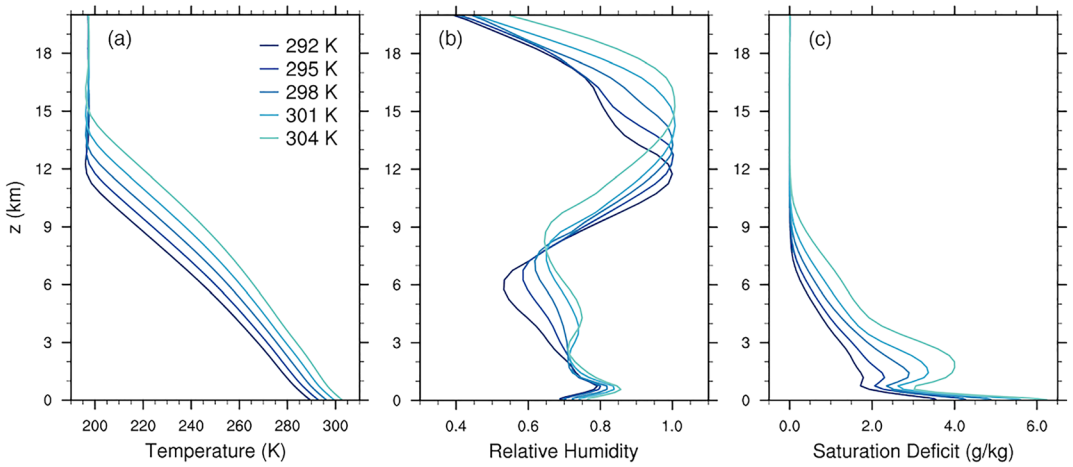

Figure 1. Steady-state profiles of (a) temperature (K), (b) relative humidity, and (c) saturation deficit (g kg^{-1}) computed from small-domain (392 km × 392 km) RCE states (Days 70–100).

analogous small-domain simulation (392 km × 392 km × 25 km) forced with the same SST but with f set to zero. A state of radiative-convective equilibrium (RCE) is attained in the nonrotating small-domain simulations after about 50 days, and the convection remains disaggregated through 100 days. The initial conditions for the TC simulations are taken from the small-domain profiles of temperature and specific humidity averaged horizontally and over Days 70 to 100 (Figure 1). To this horizontally homogenous initial condition, small amplitude (0.25 K) potential temperature perturbations are added randomly throughout the domain to break the initial homogeneity. These perturbations differ between ensemble members, allowing for a different evolution of convection in each case.

TC genesis is defined here as the first time at which the hourly maximum azimuthal-mean tangential velocity (V) reaches or exceeds 15 m s^{-1} at the lowest model level (i.e., 25 m) and maintains this threshold for at least 6 hr. The time series of V are first smoothed using a 7-point (i.e., 6-hourly) running mean. This threshold corresponds roughly to the time at which the maximum azimuthal winds transition to be rooted in the boundary layer, rather than in the midlevels like in most precursor TC disturbances (e.g., Bister & Emanuel, 1997; Raymond et al., 2011; Ritchie & Holland, 1997). We also define the time at which a precursor "seed" disturbance forms as the first time that the surface pressure anomaly first reaches or exceeds −4 hPa moving backward in time from genesis. The time series of hourly minimum surface pressure used for determining the seed time is first smoothed with a 7-point running mean. Here and throughout this manuscript, the azimuthal mean is defined as the mean of all grid points that lie in an annulus of width 4 km centered on a given radius r, where r is defined as the shortest distance to the storm center, taking into account the doubly periodic geometry of the domain. The storm center is taken as the location of the minimum value of the surface pressure field after the application of a 9-point smoother 30 times (Chavas, 2013). The position of this minimum in the smoothed surface pressure field is estimated through linear interpolation of its gradient in x and y.

PI is calculated following a revised version of the algorithm developed by Bister and Emanuel (2002) (the FORTRAN code can be obtained here: ftp://texmex.mit.edu/pub/emanuel/TCMAX). The ratio of surface exchange coefficients of enthalpy and momentum C_k/C_d within the PI code is set to 0.5, which is consistent with the simulated values of C_k/C_d near peak intensity of TCs in the model. Dissipative heating is switched on, and parcel buoyancy is computed assuming pseudo-adiabatic ascent. To provide context for the model-calculated V_p, monthly mean PI was also calculated from ERA-Interim reanalyses for the period 1981–2010 using the same settings as applied to CM1. The annual-mean "warm-pool" V_p (i.e., V_p where SST ≥ 26.5°C) from the reanalysis is 61 m s^{-1}, with the corresponding mean SST being 28.2°C (301.4 K). The steady-state V_p from the 301 K small domain simulation is 62.6 m s^{-1}, similar to the warm-pool V_p in ERA-Interim. The rough correspondence in V_p between the model RCE state and reanalysis for similar SSTs suggests that the combination of radiative cooling rate, surface fluxes, and other model settings yield a background thermodynamic state that is in some ways similar to the real-world tropics.

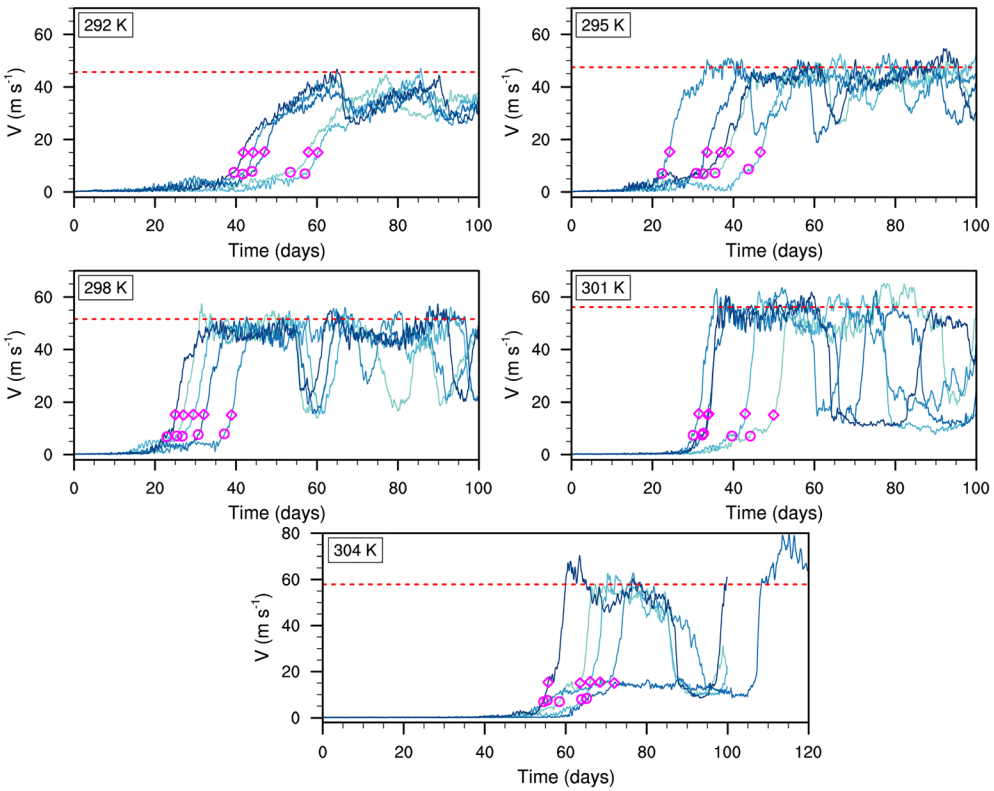

Figure 2. Time series of maximum azimuthal-mean tangential velocity at the lowest model level (V; m s^{-1}) for SSTs from 292 to 304 K, as labeled. Dark to light colors indicate individual ensemble members. The magenta circles mark the seed times (see text), and the magenta diamonds indicate the time of genesis, when V first reaches or exceeds 15 m s^{-1} (see text for details). The dashed red lines give the potential intensities for each ensemble, taken from the ensemble-mean state 5 days prior to seed time.

3. Evolution to TC Genesis

3.1. TC Seeds and GPIs

Spontaneous TC seed disturbances occur in all 25 simulations over the full range of SSTs tested (from 292 to 304 K), with the time to seed varying from 22.3 days (295 K) to 65.2 days (304 K) (Figure 2). A single TC develops in each case (Figure 3). The seeds typically manifest as broad midlevel vortices, with maximum circulation between 3 and 5 km, the radius of maximum winds between 150 and 300 km, and peak azimuthal-mean winds of about 10 m s^{-1}. An example of this structure is shown in Figure 4a for one simulation at 301 K. The variability of time to seed, from $t = 0$, within each five-member ensemble at a given SST is relatively small (σ ranges from 4.8 days at 304 K to 7.7 days at 292 K). The difference between the shortest and longest seed times when averaged across the ensembles is only 16 days. This is roughly half the internal variability found by Wing et al. (2016) based on their time to genesis metric and the same number of ensemble members, although their study only considered a single value of SST. The reduced stochasticity of spontaneous seed times here may be due to a number of factors, including the use of a different model and a fixed radiative cooling rate rather than an interactive radiation scheme. Notably, in our simulations, convective self-aggregation and subsequent TC genesis occur *without* interactive radiation across the full range of SSTs; in other words, interactive surface-fluxes alone are sufficient to excite organized convection and TC genesis. This differs from the results of Davis (2015), who found that rotating self-aggregation did not occur out to 80 days when using Newtonian cooling in the same model (noting that Newtonian cooling, while being just as simple, is not directly comparable to the constant cooling scheme applied here). Indeed Wing et al. (2016) showed that radiative feedbacks are not strictly necessary for spontaneous TC genesis, but they did help to accelerate the process, particularly longwave feedbacks. This was confirmed by Muller and Romps (2018), who showed that radiative feedbacks accelerated cyclogenesis by a factor of 2 or larger.

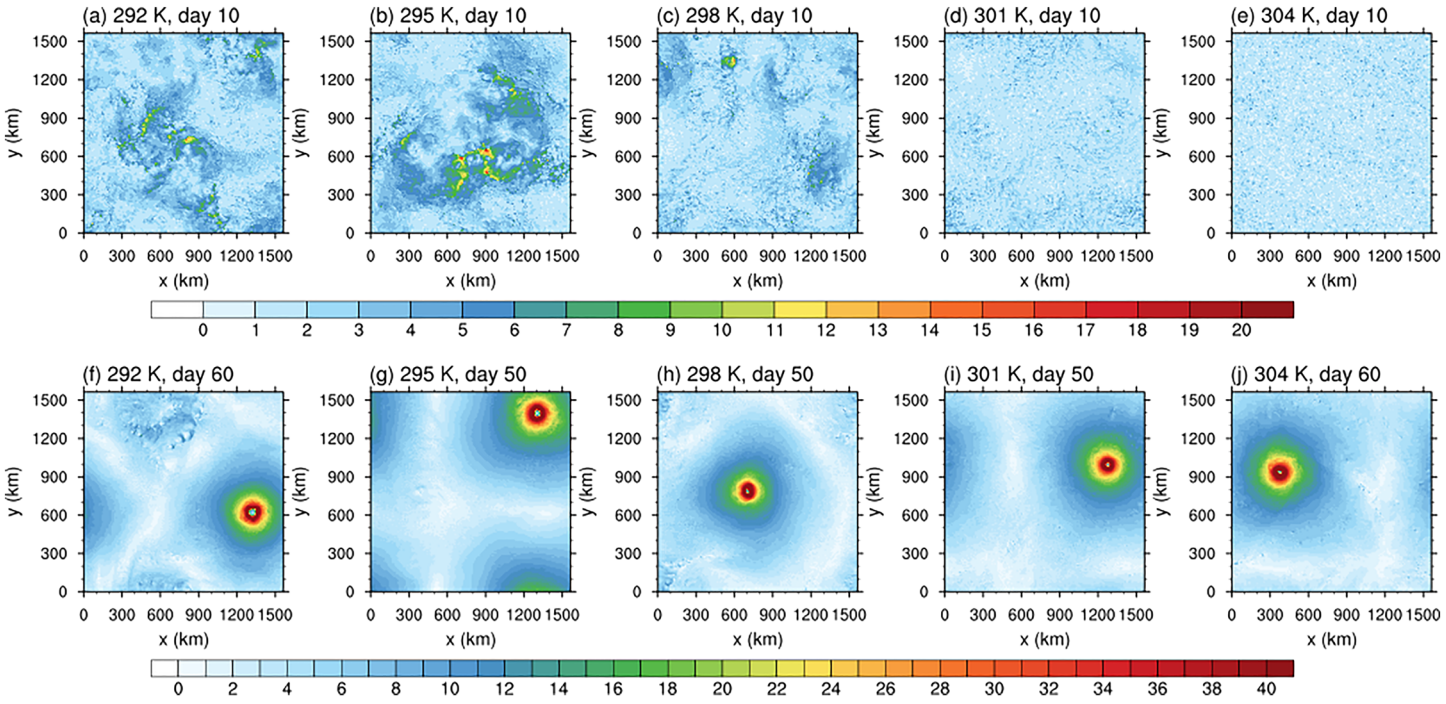

Figure 3. Snapshots of 10-m wind speed (m s^{-1}) for SSTs from 292 to 304 K (left to right), at Day 10 (a–e) and during the mature stage of TCs (f–j). Note the two different color scales for top and bottom panels. The color bar for panels (a) to (e) is capped at 20 m s^{-1} to highlight surface wind speed variability and convective gustiness at Day 10.

Turning now to TC seed time and its sensitivity to the background state, the average time for a precursor seed disturbance to form from $t = 0$ exhibits a distinctive nonmonotonic trend with increasing SST (Figure 5). The most favorable environment for seed formation occurs at 298 K, the middle value of SST, with increasingly longer seed times occurring at lower and higher SSTs. It takes about twice as long for seeds to form at 304 K ($\mu = 59.5$ days) than at 298 K ($\mu = 28.6$ days). Seed formation is also delayed as SST is decreased from 298 to 292 K ($\mu = 47.1$ days at 292 K). The delayed evolution to seed with increasing SST above 298 K is qualitatively consistent with expectations from a range of models (i.e., fewer storms in warmer climates), including GCM projections of TC-like vortices, idealized aquaplanet simulations (e.g., Merlis et al., 2016), limited-area CRM

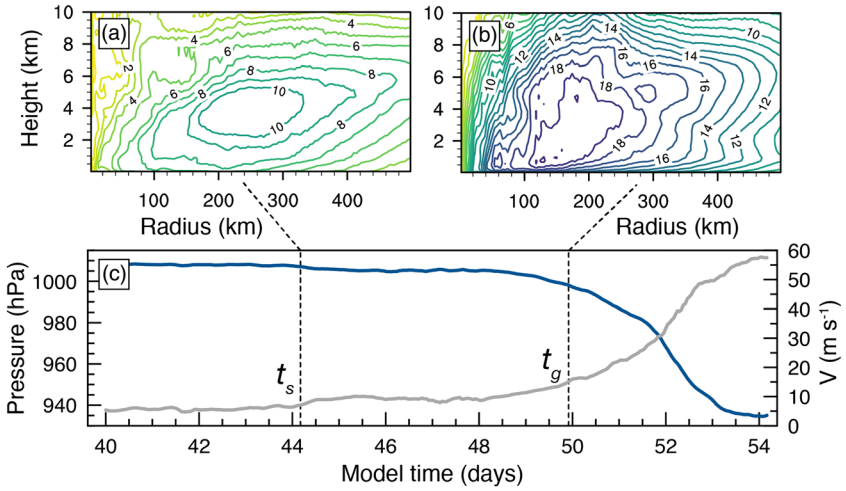

Figure 4. (a, b) Radius-height cross sections of azimuthally averaged tangential wind speed (V; m s^{-1}) at the time of (a) a precursor seed disturbance and (b) TC genesis for one simulation at 301 K. (c) Corresponding time series of minimum surface pressure (hPa; blue curve) and V (m s^{-1}; gray curve). The dashed vertical lines indicate seed (t_s) and genesis times (t_g), respectively.

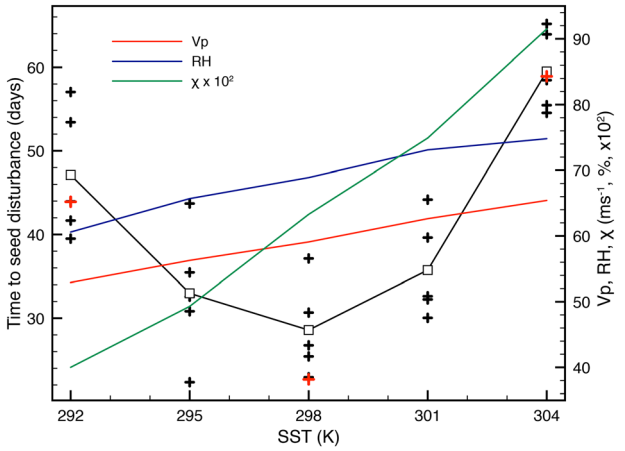

Figure 5. Time to a precursor TC seed disturbance as a function of SST (black crosses; squares show ensemble means). Solid colored lines show corresponding trends of potential intensity V_p (red), relative humidity RH (blue), and saturation deficit χ (green) taken from the small-domain RCE states. The red crosses indicate the seed times for three simulations with double the domain size (3,136 km × 3,136 km) at 292, 298, and 304 K.

simulations (e.g., Khairoutdinov & Emanuel, 2013), and model configurations that fall somewhere in between (Held & Zhao, 2008). The response of TC seed frequency (as opposed to genesis frequency) to global warming in GCMs has gained recent attention in the literature; however, thus far, there is no consensus agreement on future trends, with some studies suggesting an increase in the number of seeds with warming (e.g., Vecchi et al., 2019) and others a decreasing trend (e.g., Sugi et al., 2020).

To assess the influence of domain size on the seed times, three sensitivity experiments were performed in which the lateral size of the domain was doubled from 1,568 to 3,136 km for SSTs of 292, 298, and 304 K. Because TC size in RCE on an *f*-plane is expected to scale as V_p/f (Chavas & Emanuel, 2014; Cronin & Chavas, 2019; Emanuel, 1995; Held & Zhao, 2008) and V_p increases with increasing SST here, the 304 K case is expected to have the most limiting domain size, potentially impacting the emergence time of a seed. The overall trend of seed times for the larger domain experiments is very similar to the control simulations (see red crosses in Figure 5), with a clear minimum at 298 K flanked by longer seed times at 292 and 304 K. At the lowest SST of 292 K, three distinct vortices formed initially around Days 45–55 (though we did not run it long enough to reach statistical equilibrium), whereas only a single storm formed at 298 and 304 K. The formation of multiple vortices at 292 K is consistent with the inverse relationship between the total number of TC-like vortices in a limited-area, doubly periodic domain and the surface saturation specific humidity found in previous work (Khairoutdinov & Emanuel, 2013, their Figure A2). Ideally, one would perform a full five-member ensemble at this larger domain size, but we found the associated computational costs prohibitive.

Returning to our baseline set of simulations, the nonmonotonic trend in seed times is evaluated against variations in traditional thermodynamic genesis potential parameters (Figure 5), namely, PI V_p, midlevel relative humidity RH (evaluated at 600 hPa), and the normalized saturation deficit χ:

$$\chi \equiv \frac{s_b - s_m}{s_0^* - s_b}$$

χ is evaluated using the moist entropies at 600 hPa (s_m) and at the lowest model level (s_b), respectively, and the saturation moist entropy of the sea surface (s_0^*), all of which are calculated from the small-domain RCE states.

V_p, midtropospheric RH, and χ all exhibit monotonic increases with increasing SST and therefore cannot independently explain the "U" shape of the seed times in Figure 5. The decreasing time to seed from 292 to 298 K is consistent with increasing values of V_p and RH, but seed formation becomes increasingly delayed from 298 to 304 K despite the same positive trends in V_p and RH. This delay is arguably due to the larger saturation deficit with warming (e.g., Mallard et al., 2013; Rappin et al., 2010; Tang et al., 2016), but the χ trend alone is insufficient to explain the behavior of the "U" shape. The relatively fast evolution to seeds at 298 K is possibly due to some optimal combination of V_p and χ, both of which increase with warming (ignoring other factors that may affect local circulations, such as cold pools and convective gustiness).

We now evaluate two commonly used GPIs, described below, to see if the combination of V_p and humidity (either RH or χ) may help to explain the nonmonotonic response of seed times to warming. The seed evolution period is first inverted to obtain a simulated seed rate having the same units as GPI (i.e., a number per unit time). The first GPI is that of Emanuel and Nolan (2004) (introduced earlier as GPI-EN04) and is expressed as

$$\mathrm{GPI-EN04} = \left|10^5\eta\right|^{\frac{3}{2}}\left(\frac{RH}{50}\right)^3\left(\frac{V_p}{70}\right)^3(1+0.1V_{shear})^{-2} \quad (2)$$

where η is the mean absolute vorticity at 850 hPa, RH the relative humidity at 600 hPa, V_p the PI in terms of wind speed, and V_{shear} the mean absolute vector difference of winds at 850 and 200 hPa. In our setup,

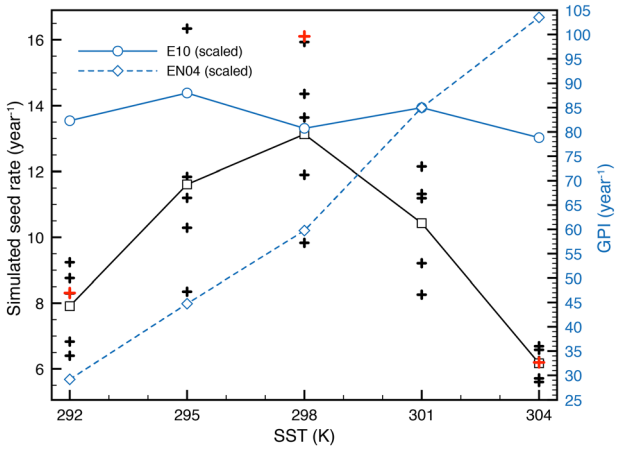

Figure 6. Simulated seed rates (i.e., $1/t_s$) (black crosses; squares show ensemble means) as a function of SST, and corresponding scaled GPIs of Emanuel and Nolan (2004) (diamonds, blue dashed line) and Emanuel (2010) (circles, blue solid line) calculated from the small-domain RCE states. The rate of seed formation and the GPIs have been scaled to give a number per year. The red crosses indicate additional sensitivity simulations as described in Figure 5.

V_{shear} is negligibly small such that the last term on the RHS is unity, and η is just the background planetary vorticity f, which is fixed at 5×10^{-5} s^{-1}.

The second GPI was developed by Emanuel (2010) (hereafter, GPI-E10) to account for factors that are themselves expected to vary with climate warming and is expressed as

$$\mathrm{GPI-E10} = |\eta|^3 \chi^{-\frac{4}{3}} MAX\left(\left(V_p - 35\ \mathrm{m\ s^{-1}},\ 0\right)^2 \left(25\ \mathrm{m\ s^{-1}} + V_{shear}\right)^{-4}\right) \quad (3)$$

where χ is the nondimensional saturation deficit, defined earlier, and replaces the RH in 2. Note that in the absence of η, 3 resembles the theoretically based ventilation index of Tang and Emanuel (2012), which has been used to understand aspects of the observed spatiotemporal distribution of TC genesis (e.g., Hoogewind et al., 2020) as well as TC genesis and intensification in CMIP5 models (Tang & Camargo, 2014). We return to the ventilation index in section 3.2.

When 2 and 3 are evaluated for the small-domain RCE states, we find that neither GPI-EN04 nor GPI-E10 is able to capture the distinctive nonmonotonic behavior of the explicitly simulated seed rates (Figure 6). The magnitudes of these GPIs are arbitrary, so we scale them to give a rate of 85 TCs per year at 301 K, similar to the current climate. GPI-EN04 increases considerably with warming, more than tripling in magnitude from 292 to 304 K, which is qualitatively consistent with multimodel mean projections of GPI-EN04 in CMIP5 models under the RCP 8.5 scenario (Camargo, 2013). GPI-E10, on the other hand, exhibits much less sensitivity to warming, varying between about 80 and 90 per year due to compensating influences of increasing V_p and increasing χ. The relatively small variation of EN10 with warming is consistent with results obtained by Camargo et al. (2014), who showed that the use of saturation deficit (rather than RH) in GPIs successfully captured the global decrease of TC frequency with warming as simulated by GFDL's HiRAM model but that this decrease was offset by increasing PI. In summary, neither of the two GPIs tested reproduce the change in seed rate with climate warming in our simulations.

3.2. TC Incubation Period and GPIs

We now shift to the second stage of TC evolution in our simulations and assess the time between a TC seed and subsequent cyclogenesis (the "incubation period," following Rappin et al., 2010) and its response to surface warming. An example of the incubation period is illustrated for a single simulation at 301 K in Figure 4. It represents a structural change from the maximum azimuthal circulation being situated aloft as a midlevel vortex during or close to the seed time (which we define using minimum surface pressure; section 2.2) to the strongest winds occurring near the surface at genesis as is typical in warm-cored systems. The minimum surface pressure falls by about 9 hPa from seed to genesis (Figure 7) across SSTs. For the 301 K SST ensemble, which is close to the current climate, the minimum surface pressure at seed time is ~1,007 hPa (similar to tropical depressions) and ~998 hPa at genesis.

The incubation period shows less systematic dependence on SST compared to the seed gestation period (Figure 7), although, on average, the shortest incubation occurs at 298 K (1.9 days) and the longest at 304 K (5.6 days). There is also a tendency for an increased variance of incubation for SSTs > 298 K, which is particularly evident at 304 K, where the incubation time ranges from just over 1 day to 13 days (implying that genesis may become less predictable in a warmer climate).

The dependence of incubation times on GPI-relevant thermodynamic variables is evaluated as in the previous section, but for this analysis, V_p, χ, and RH are calculated from a 5-day mean state prior to seed time in each simulation, rather than the RCE state. The reason for this is that the environment tends to drift from the RCE state with time (for instance, the boundary-layer humidifies as the simulations evolve due to stronger surface winds, reducing the air-sea disequilibrium and thus V_p) so that the mean-state closer to seed/genesis is more relevant for understanding the relationship between incubation times and GPIs. In

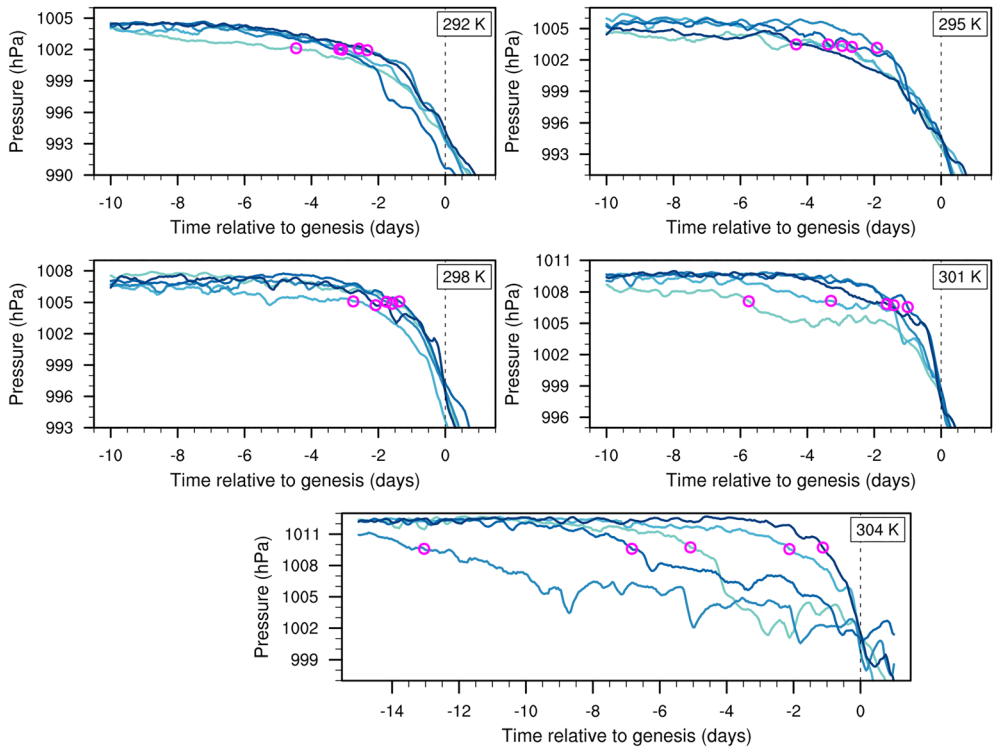

Figure 7. Time series of hourly minimum surface pressure given by the TC center finding algorithm for days prior to TC genesis as indicated on the abscissae. The magenta circles indicate the seed times for each simulation. The series have been smoothed using a 7-point (i.e., 6-hourly) moving average.

addition to GPI-EN04 and GPI-E10, the inverse of the ventilation index (Λ^{-1}) (Tang & Emanuel, 2012) is also assessed in relation to incubation time. The ventilation index Λ has both theoretical and empirical connection to the probability of genesis and is defined as

$$\Lambda = \frac{V_{shear}\chi_m}{V_p}$$

where χ_m is the (nondimensional) entropy deficit, and V_p and V_{shear} are as defined earlier. The entropy deficit has the same formulation as the normalized saturation deficit χ, except that the denominator $(s_0^* - s_b)$ is evaluated at the radius of maximum winds for a TC at its PI. Our simulations have no imposed large-scale shear, by design, but setting V_{shear} to zero in Λ would result in zero ventilation for all simulations, so we set V_{shear} to a nominally small value of 1 m s^{-1} (i.e., Λ for this analysis is just the ratio of χ_m/V_p). We note that our choice of constant value of 1 m s^{-1} for V_{shear} is arbitrary; choosing a different constant would simply rescale all values of Λ uniformly but does not affect the interpretation of results here.

Although our primary focus is on the ensemble-mean behavior of incubation time and its dependence on the mean background state, we consider now briefly the intraensemble variability of incubation periods. This analysis is motivated by the inherent variability of V_p, χ, and RH in the lead up to seed time, even when SST is held constant. The relationship between incubation periods at each SST and GPI thermodynamic variables (V_p, χ, and RH) is displayed in Figure 8 as a series of simple scatter plots. Except for 304 K, the relationship between incubation and GPI-relevant variables is as one might expect (Rappin et al., 2010): Longer incubation times are associated with lower values of V_p and RH and higher values of χ (e.g., Tang et al., 2016). Note that V_p varies by as much as 10% for the same value of SST, highlighting the importance of variations in surface wind speed for determining V_p (not shown).

Turning to the dependence of incubation time on the GPIs for a given SST, it is clear from Figure 9 that longer incubation periods are associated with lower values of GPI (except at 304 K) and vice-versa. In fact,

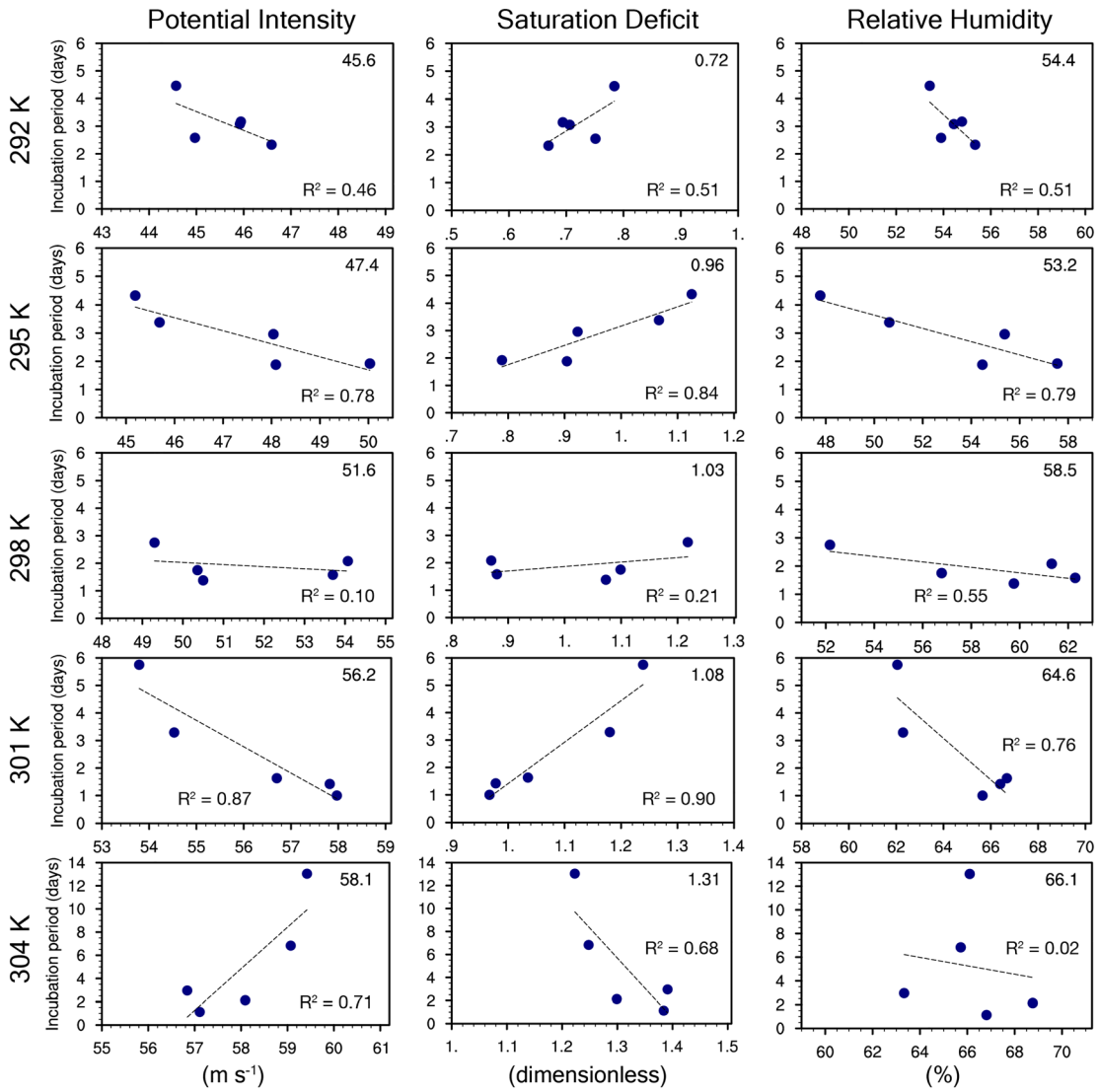

Figure 8. Scatter plots showing the relationship between TC incubation period at each SST (rows) and GPI-relevant thermodynamic variables: (i) potential intensity V_p (first column), (ii) normalized 600-hPa saturation deficit χ (second column), and (iii) 600-hPa relative humidity. The GPI variables are calculated from a 5-day mean state prior to the seed time. The ensemble-mean values of V_p, χ, and RH are shown in the top right of the corresponding panels. The linear least squared regression fit is indicated by the dashed lines, along with the corresponding variance explained values (R^2).

all three GPIs tested (GPI-EN04, GPI-E10, and Λ^{-1}) have very similar relationships with the incubation time; they just differ in their magnitudes due to different weights employed for V_p, χ, and RH in their formulations.

The overall dependence of incubation time on SST is assessed by examining the relationship between the ensemble-mean GPIs and the ensemble-mean inverse of the incubation period (i.e., a number per unit time). The most favorable environments for genesis (i.e., shorter incubation times) occur at 298 and 301 K (Figure 10), with less favorable environments at SSTs above and below these values. Both GPI-EN04 and GPI-E10 track the explicitly simulated incubation behavior reasonably well between 292 and 301 K, but there is a notable divergence in the GPIs as SST increases further to 304 K. GPIs that depend on saturation deficit (E10 and Λ^{-1}), which increases by 21% between 301 and 304 K, mimic the explicitly simulated longer incubation times at 304 K, whereas EN04 continues to increase due to its dependence on RH. The divergence of the χ and RH-dependent GPIs between 301 and 304 K is consistent with recent work by Lee et al. (2020), who showed a similar divergence of GPIs with warming in GCMs depending on whether χ or RH was used

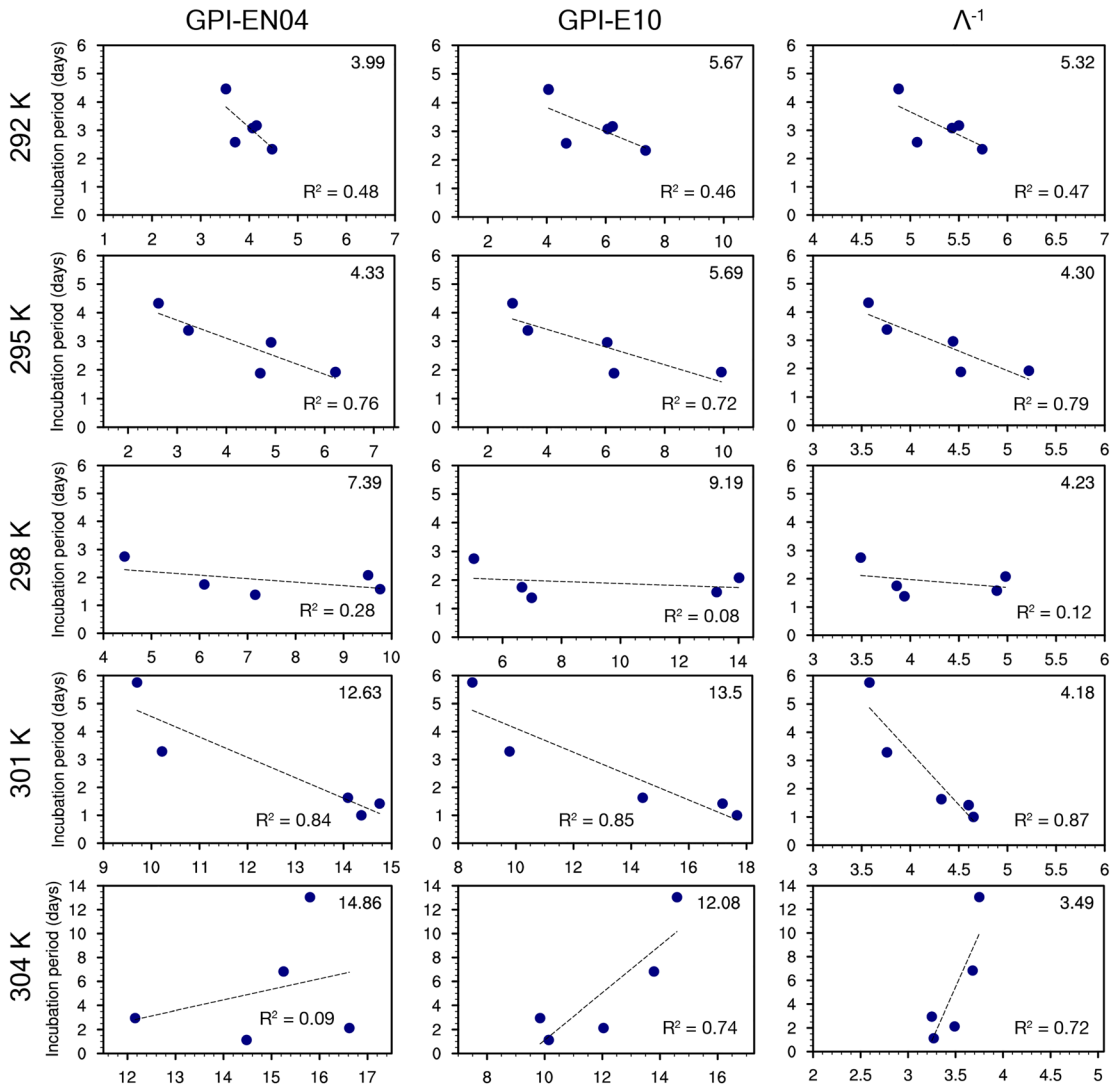

Figure 9. As in Figure 8 but for the relationship between TC incubation period and GPI: (i) EN04 (first column), (ii) E10 (second column), and (iii) inverse of the TE12 ventilation index (Λ^{-1}). The ensemble-mean GPIs are shown in the top right of each panel and are scaled to give similar magnitudes.

for midtropospheric moisture variable. Finally, we note the large-domain sensitivity experiment at 298 K results in an incubation period that is longer and outside of the ensemble spread for the standard domain setup, suggesting that this metric may be sensitive to the choice of domain size.

3.3. Evolution of Humidity During TC Development

Previous studies of tropical cyclogenesis have demonstrated that an important process associated with the strengthening of incipient vortices into TCs is the moistening of the inner-core region of the storm (e.g., Bister & Emanuel, 1997; Nolan, 2007). Furthermore, studies of spontaneous TC formation in RCE have found that TC genesis coincides with an amplification of the spatial variance of column-integrated moist static energy (e.g., Muller & Romps, 2018; Wing et al., 2016), indicating an increase in the horizontal variability of moisture within the domain. These results suggest that examining the evolution of the humidity distribution may provide further insight into the factors controlling genesis and seed times in our simulations.

Figure 11 shows time series of maximum azimuthal windspeed and lower-tropospheric (z = 2–6 km) RH within the core region of the storm around the time of genesis. Here, the core of each storm is defined as the region within 100 km of the storm center, with the storm center defined by the surface pressure minimum, as described in section 2. At genesis time, the ensemble-mean RH within the core is 25–40% higher

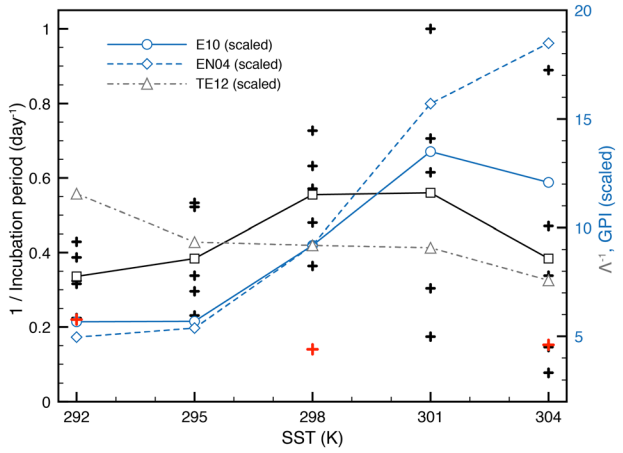

Figure 10. Simulated incubation rates (i.e., 1/incubation period) (black crosses; squares show ensemble means) as a function of SST, and corresponding scaled GPIs of Emanuel and Nolan (2004) (diamonds, blue dashed line) and Emanuel (2010) (circles, blue solid line). The inverse of the ventilation index (Λ^{-1}; TE12; gray dashed line) is plotted for comparison. The GPIs and Λ^{-1} are calculated over a 5-day mean state prior to the start of the incubation period. E10 and Λ^{-1} are scaled to give the same value as EN04 at 298 K for plotting purposes. The red crosses indicate additional sensitivity simulations as described in Figure 5.

than the domain mean across the different SSTs. This is due to both a local increase in RH near the storm center and a decrease in the domain-mean RH that occurs as the storm begins to intensify.

Positive anomalies of RH in the core also exist prior to genesis; for all SSTs, most ensemble members show anomalies of RH in the storm core of at least 5% at the seed time t_s. These moist anomalies coincide with an increase in the domain-wide specific humidity variance in the lower troposphere (Figure 11, green lines), which, at most SSTs, begins to increase a few days prior to genesis.

The above results suggest that changes to the humidity variability in the domain are important precursors to TC genesis, consistent with the previous studies of spontaneous cyclogenesis in rotating RCE (Muller & Romps, 2018; Wing et al., 2016) and convective aggregation in nonrotating RCE (Wing & Emanuel, 2014). A plausible hypothesis is then that the time to genesis is controlled by this humidity variability; a seed disturbance requires moisture anomalies of sufficient size in order to form, and such moisture anomalies must be produced through the feedback mechanisms described by Wing and Emanuel (2014) in their moist static energy variance budget analysis.

To investigate the above hypothesis, we examine in detail a single ensemble member of the case with SST equal to 298 K (Figure 12). In this ensemble member, the seed disturbance forms just prior to Day 23, with genesis occurring roughly 2 days later. As expected, the inner core of the developing cyclone is anomalously moist in the lower troposphere, both at genesis and at seed time. On the other hand, 2 days prior to seed time, the lower-tropospheric humidity anomaly in the vicinity of the pressure minimum is close to zero, despite the fact that there appears to be a coherent, but weak, vortex developing in the low-level wind speed. Indeed, the moistest regions of the atmosphere occur far away from the region occupied by the incipient vortex.

The evolution in Figure 12 provides hints that positive moisture anomalies may not always be required in the very early stages of the development of an incipient vortex within the context of our RCE simulations. While our analysis is not conclusive, it suggests that increases in moisture variability may not be the dominant control on seed time. Ideally, we would perform a similar analysis for all simulations, but we did not have high enough temporal-resolution data saved in all cases. Other potentially important factors include the buoyant production of available potential energy (APE) within the boundary layer, which has recently been argued to be important for nonrotating convective aggregation in RCE (Yang, 2018). Buoyancy fluxes and turbulence kinetic energy within the boundary layer are found to decrease monotonically with warming in our simulations in association with the increasing dominance of latent heat fluxes over the sensible heat flux at the surface (not shown). Further work is required to determine if this surface temperature dependence of the strength of boundary-layer turbulence has any influence on the time to genesis and its variations with SST, although clearly it cannot, on its own, account for the nonmonotonic variation of genesis time with SST.

4. TC Intensification

4.1. TC Lifetime Maximum Intensity

We now transition from genesis to the intensification phase following genesis, including the response of maximum intensity and intensification rate to surface warming in our idealized framework. TC lifetime maximum intensity V_{max} is defined here as the maximum value of the azimuthal-mean tangential wind at the lowest model level over the lifetime of a storm. The ensemble-average maximum intensity $<V_{max}>$ increases with increasing SST from 46.1 m s^{-1} at 292 K to 64.8 m s^{-1} at 304 K (excluding one case at 304 K where rapid intensification does not occur until several weeks after genesis; Figure 2). V_p, which is calculated from a 5-day mean state prior to seed time, is a reasonably accurate upper-bound of $<V_{max}>$ at the lowest SST of 292 K but underestimates $<V_{max}>$ for SSTs $\geq$ 298 K (Figure 2). Notably, the 292 K intensification curves

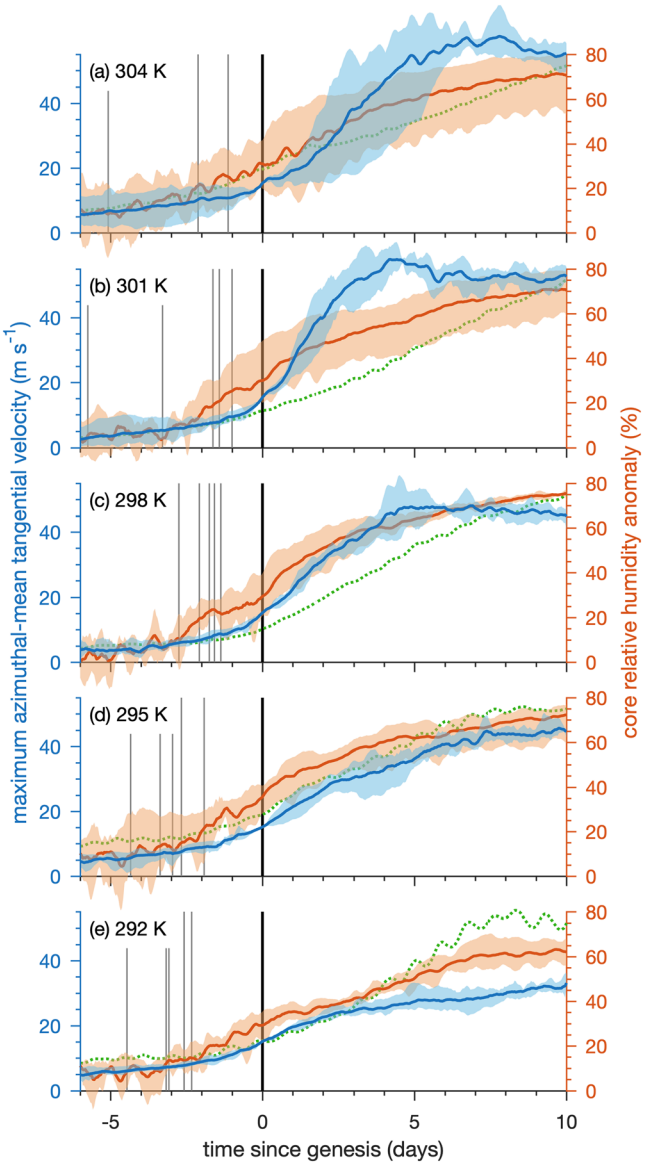

Figure 11. Composite time series of maximum azimuthal-mean tangential velocity at the lowest model level (V; blue, left axis) and lower-tropospheric relative humidity anomaly in the storm core (mass-weighted mean between 2 and 6 km and within 100 km of the storm center) relative to the domain mean (orange, right axis) centered on the time of genesis (t_g; vertical black lines) for simulations with SSTs of (a) 304 K, (b) 301 K, (c) 298 K, (b) 295 K, and (e) 292 K. Lines give the ensemble mean and shading represents the range across the ensemble; one ensemble member at 304 K is omitted because it does not intensify immediately after genesis. Vertical gray lines show the seed time t_s of each ensemble member, and green dashed line shows ensemble-mean humidity variance $\overline{q'^2}$ averaged over the lower-troposphere and scaled to reach the same value 10 days after genesis in each panel.

exhibit a very slow intensification phase soon after genesis such that V_{max} is not attained until several weeks later. If we restrict $<V_{max}>$ to the first 15 days after t ($V_{max}/2$), then the storms at 292 K undershoot V_p by ~6 m s^{-1}, with an increasing tendency for $<V_{max}>$ to overshoot PI for SSTs > 298 K. The physics of the very slow intensification at 292 K are not immediately apparent. One might expect a relatively dry middle-troposphere to reduce the maximum entropy available to the TC (e.g., Braun et al., 2012; Cronin & Chavas, 2019; Tang & Emanuel, 2010); however, in the present case, the numerator of the entropy deficit term in Λ, $(s_b - s_m)$, is smallest at 292 K. Normalization of the intensity by V_p at various stages as the TC evolves (e.g., Tang & Emanuel, 2012) may be needed to get a clearer picture of the relationship between Λ and $<V_{max}>$ and/or intensification rate. The PI itself is, however, well correlated with the maximum intensification rate, as will be demonstrated in the next section.

4.2. TC Intensification Rate

In recent years, the topic of TC rapid intensification (RI, defined as an increase in TC intensity of at least 30 kts (15.4 m s^{-1}) over a 24-hr period) has gained much attention for several reasons, including because RI events tend to be associated with the largest intensity forecast errors and because storms exhibiting RI have been suggested to become more frequent in a warmer climate (e.g., Bhatia et al., 2018; Emanuel, 2017). There is some evidence that TC intensification rates and/or the proportion of RI events have already increased in some regions of the world since the 1980s, including in the North Atlantic (e.g., Balaguru et al., 2018; Bhatia et al., 2019) and the Western North Pacific (Kang & Elsner, 2019).

The effect of surface warming on the maximum intensification rate (ΔV_{max}) of our simulated TCs is quantified here using composites of the maximum tangential wind for a 20-day period relative to t ($V = V_{max}/2$), during the maximum intensification phase (Figure 13a). As noted in the previous section, one simulation at 304 K does not intensify rapidly until several weeks after genesis (Figure 2) and appears to be an outlier in terms of its extreme intensification rate and small size, so we discard it for the remainder of this section. ΔV_{max} is defined as the largest 24-hr change in V during any stage of the initial genesis/intensification period (Figure 13a), and the ensemble-mean of this metric increases monotonically with warming from 9 m s^{-1} day^{-1} at 292 K to 24.1 m s^{-1} day^{-1} at 304 K. The increase in ΔV_{max} scales more or less linearly with increasing PI V_p ($R^2 = 0.99$) (Figure 13b) at a rate of roughly 1.2 m s^{-1} day^{-1}/m s^{-1}. An almost identical linear relationship is obtained by replacing V_p with the surface moisture disequilibrium $(q^* - q)$ (e.g., Črnivec et al., 2016). Furthermore, storms that achieve or exceed RI (i.e., generally for SSTs $\geq$ 298 K in our setup; Figure 13b) are more likely to reach or exceed their PI. This suggests that, neglecting changes in the circulation (that may affect shear, dry air, etc.), thermodynamic factors tend to increase the intensification rates of TCs under warming, in line with recent results from GCM projections (e.g., Bhatia et al., 2018; Emanuel, 2017).

More generally, two theories currently exist that predict the full temporal evolution of the intensification of a TC toward its maximum PI. We revisit and extend them here for the purpose of directly testing their predictions against our simulation results.

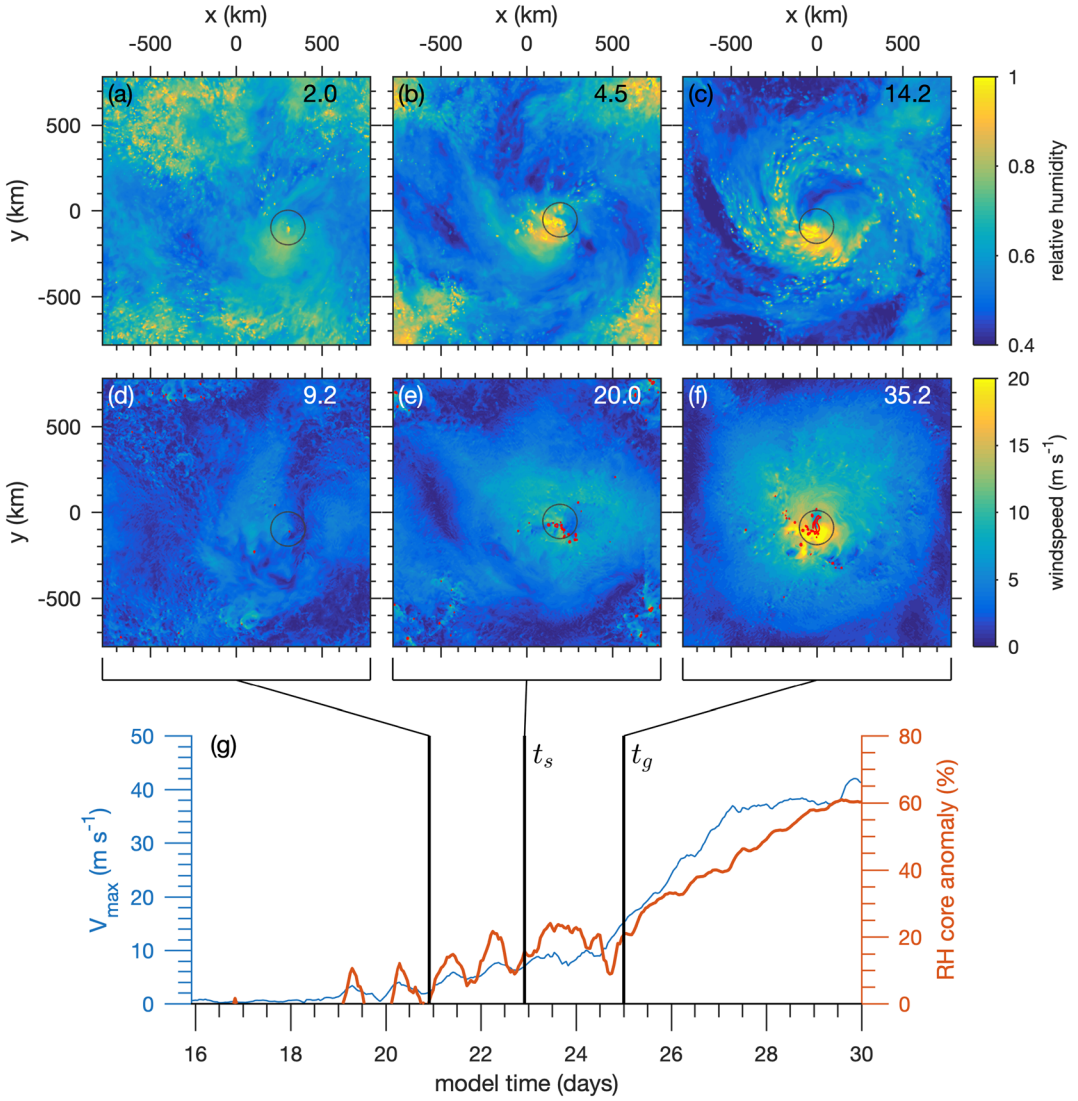

Figure 12. Snapshots of (a–c) lower-tropospheric relative humidity (mass weighted mean between 2 and 6 km) and (d–f) windspeed (colors) and vorticity (red contour marks value of 10f) at the lowest model level for (a, d) 2 days before seed time, (b, e) seed time t_s, and (c, f) genesis time t_g in a single ensemble member in which SST = 298 K. Panel (g) shows time series of maximum azimuthal-mean tangential velocity at the lowest model level (V; blue, left axis) and lower-tropospheric relative humidity anomaly in the storm core (within 100 km of the storm center, marked by black circles on panels (a)–(f)) relative to the domain mean (orange, right axis) for the same ensemble member. Black vertical lines show the times of each snapshot. Numbers give (a–c) the magnitude of the minimum surface pressure anomaly (hPa) and (d–f) the mean-squared windspeed at the lowest model level ($m^2\ s^{-2}$) for the corresponding snapshot.

First, Emanuel (2012) provides an explicit time-dependent solution for storm intensification (E12 Equation 19) given by

$$\tilde{v}_{E12}(t) = \tanh\left(\frac{t}{\frac{2h}{C_k v_p}}\right) \tag{4}$$

where $\tilde{v} = \frac{v}{v_p}$ is the maximum wind speed as a fraction of the PI, C_k is the surface enthalpy exchange coefficient, and h is the fluid depth. This prediction emerges from the posited role of small-scale turbulence in setting the evolution of the vertical stratification of the near-storm outflow, which in turn sets the radial

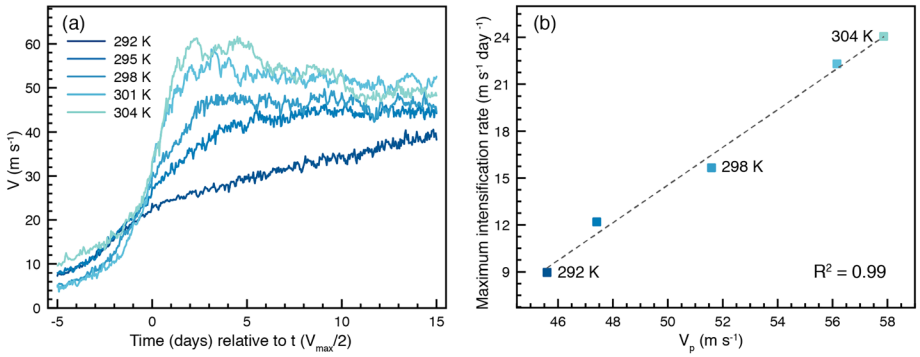

Figure 13. (a) Ensemble-mean evolution of maximum azimuthal-mean tangential velocity (V) at the lowest-model level, relative to time of $V_{max}/2$. (b) Mean maximum 24-h intensification rate plotted against the corresponding potential intensity (V_p) for each SST. V_p is calculated from a 5-day mean state prior to seed time. The linear least squared regression fit is shown by the dashed line, along with the corresponding variance explained value (R^2).

gradient of boundary layer entropy and thus the wind field. Equation 4 includes an intrinsic time scale given by $\frac{2h}{C_k v_p}$.

Equation 4 was derived assuming a quiescent initial condition, $\tilde{v}_{E12}(t=0)=0$. However, the solution (beginning from E12 Equation 17) may be generalized to any initial condition $\tilde{v}_{E12}(t=0)=\tilde{v}_0$, given by

$$\tilde{v}_{E12}(t)=\tanh\left(\frac{t}{\frac{2h}{C_k v_p}}+\tanh^{-1}(\tilde{v}_0)\right) \tag{5}$$

Second, the ventilation theory of Tang and Emanuel (2010, 2012) predicts intensification rates based on the net power surplus associated with the TC heat engine, accounting for the power source from surface enthalpy fluxes and the power sinks from surface frictional dissipation and the import of low-entropy environmental air by environmental wind shear ("ventilation"). Chavas (2017) rederived this power balance and then provided a theoretical solution for normalized intensity change (C17 Equation 18), $\Delta\tilde{v}$ as a function of current normalized intensity, $\tilde{v}=\frac{v}{v_p}$ and the normalized ventilation, λ, that is

$$\Delta\tilde{v}=(\tilde{v}-\lambda)^{\frac{1}{3}}-\tilde{v} \tag{6}$$

Here we show that we may take C17 theory one step further to derive a time-dependent equation for normalized intensity, whose prediction may be compared against E17. The strongest intensification rates occur for zero ventilation, the solution for which is

$$\Delta\tilde{v}=\tilde{v}^{\frac{1}{3}}-\tilde{v} \tag{7}$$

Zero ventilation is reasonable for our system, given that there is no large-scale flow and hence no large-scale vertical wind shear. In the absence of large-scale shear, small-scale convective turbulence may play a larger role in transporting low-entropy air into the storm core (Alland et al., 2017; Riemer & Laliberté, 2015), thereby yielding positive ventilation. Notably, such a process may itself be temperature-dependent, but it is much less well-understood, and so we do not address it in this work.

Ventilation theory does not provide an explicit time scale for this response, as the theory is applied only specifically at the surface at the radius of maximum winds, but the radial and vertical structure of the kinetic energy response is ambiguous. Thus, in the absence of a theory for this time scale, we may simply introduce a constant time scale, τ, in order to convert this to a prognostic equation, that is,

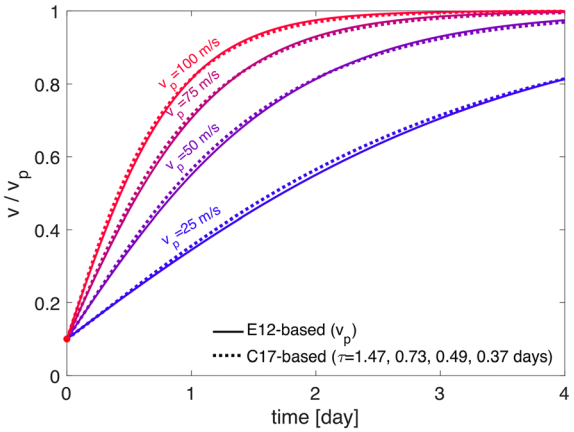

Figure 14. Comparison of predictions for intensity change from the E12-based solution (Equation 5; solid) and C17-based solution (Equation 11; dashed). E12 solutions are shown for potential intensity values of 25, 50, 75, and 100 m s^{-1}; C_k = 0.0012 to match the simulations and h = 5 km following E12. Corresponding C17 solutions are shown with time scales of 1.47, 0.73, 0.49, and 0.37 days, respectively. Note that τ scales directly with V_p^{-1}, as both simply act to rescale the time dimension in their respective equations.

$$\frac{\partial \tilde{v}}{\partial t} = \frac{\tilde{v}^{\frac{1}{3}} - \tilde{v}}{\tau} \tag{8}$$

This equation can be solved for $\tilde{v}$ to yield

$$\tilde{v} = \left(1 - C_2 e^{-\frac{2}{3}\frac{t}{\tau}}\right)^{\frac{3}{2}} \tag{9}$$

We apply as a boundary condition a weak initial vortex, $\tilde{v}(t=0) = \tilde{v}_0$, where $\tilde{v}_0 > 0$ (for $\tilde{v}_0 = 0$, $\tilde{v}$ will remain zero for all time from Equation 8). Substituting in and rearranging yields

$$C_2 = 1 - \tilde{v}_0^{\frac{2}{3}} \tag{10}$$

Thus, the final result is

$$\tilde{v}_{C17}(t) = \left(1 - \left(1 - \tilde{v}_0^{\frac{2}{3}}\right) e^{-\frac{2}{3}\frac{t}{\tau}}\right)^{\frac{3}{2}} \tag{11}$$

Note that the intrinsic time scale for the E12 solution for normalized intensity has an additional positive dependence on V_p, whereas the ventilation-based solution is invariant by imposition.

A comparison of the solutions given by the E12-based solution (Equation 5) and the C17-based solution (Equation 11) is provided in Figure 14. We start with an initial normalized intensity of $\tilde{v}_0 = 0.1$ (i.e., $v_0 = \frac{1}{10} V_p$). For the E12 solution, we show solutions for potential intensities of 25, 50, 75, and 100 m s^{-1}(note: 70 m s^{-1} is the threshold for Category 5 on the Saffir-Simpson scale). For each curve, $C_k = 0.0012$ to match our simulations, and the fluid depth is set constant to h = 5,000 m following E12. We then compare these results to corresponding C17 solutions, with the time scale set to τ = 1.47 days for V_p = 25 m s^{-1} and scaled downwards with V_p^{-1}, as both quantities simply act to rescale time in their respective equations. Doing so yields temporal evolutions that are nearly identical to E12 at all times for each of the four curves. This result is rather remarkable, as each model only has one degree of freedom (h for E12 and τ for C17), and in each case that parameter simply rescales time; hence, the temporal structures of the two solutions are fixed. Given that the two theories rest on distinct physical foundations, it is not currently known whether this is merely a coincidence or whether there exists some deeper physical connection.

It is worth briefly placing these theoretical intensification predictions in the context of observed intensification rates. Kowch and Emanuel (2015) analyzed the distribution of intensity change in the historical record and found peak 6-hourly intensification rates of approximately 24 m s^{-1} (8 kt hr^{-1}, from 6-hourly data), though this would be unlikely to persist for four consecutive 6-hr periods. Indeed, Carrasco et al. (2014) found peak 24-hourly intensity changes of approximately 50 m s^{-1} (95 kt/24 hr). The theoretical solutions increase by approximately 60% in 1 day—for a typical high-end PI of 75 m s^{-1}, this would be 45 m s^{-1}/24 hr, which is comparable to these observed values. This suggests that these models are at least qualitatively reasonable for representing rapid intensification in the real world.

We note, though, that both theoretical predictions carry significant uncertainty in their intrinsic time scale. For C17, this time scale is totally arbitrary. For E12, this time scale depends on the fluid depth, h, whose precise definition is not clear and would seem likely to vary strongly with radius. At a minimum, we may test whether there exists a dependence of the normalized intensification rate on V_p (which C17 does not predict) and, if one does exist, how the magnitude of this dependence compares with that predicted by E12 theory.

The mean normalized intensity evolutions within each experiment ensemble are displayed in Figure 15, along with the E12-based prediction of Equation 5 for each curve (dashed lines). At higher temperatures, a TC approaches its PI much more rapidly than at lower temperatures, as was found above for ΔV_{max}.

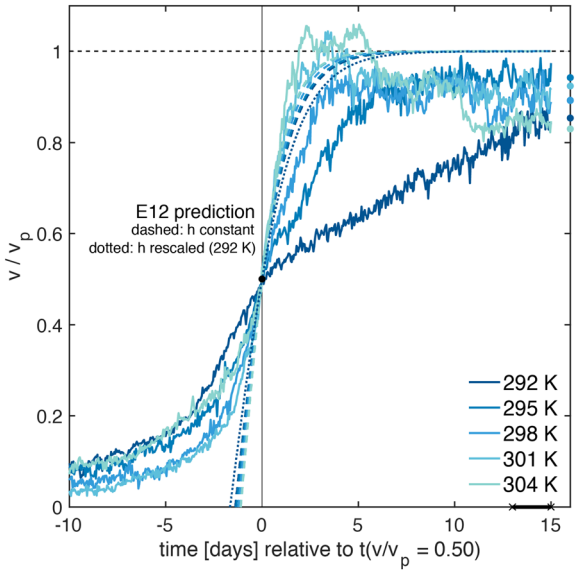

Figure 15. Mean temporal evolutions of normalized intensity across experiments (thick curves). Evolutions are centered in time on the time, t_0, at which mean normalized intensity (V_m) is 50% of its potential intensity (i.e., $\tilde{v} = 0.5$). E12-based predictions fit to $(t_0, \tilde{v}) = (0, 0.5)$ shown for constant $h = 5{,}000$ m following E12 (dashed). E12-based prediction shown for variable h for 292 K (dotted), where h has been rescaled by 1.19 to match the increase in boundary layer depth relative to 304 K. Dots on the right edge indicate the 48-hr mean value of $\tilde{v}$ averaged over days t_0+13 and t_0+14 (black line on x axis).

However, Figure 15 makes evident that this strong temperature dependence applies specifically to the second phase of the intensification process ($\tilde{v} > 0.5$), where the curves diverge strongly; intensification rates differ less strongly during the first phase ($\tilde{v} < 0.5$). Note that by Day 15, the intensities across simulations reconverge toward one another and scale closely with V_p (with the exception of 304 K, whose value is a bit lower likely due to its increased temporal variability). Hence, the behavior during the second phase of intensification appears to be similar to the transient overshoot immediately following rapid intensification, in which the intensity may exceed its PI, which has been noted in past idealized modeling studies (e.g., Chavas & Emanuel, 2014; Hakim, 2011). In our simulations, the systematic variation in this transient state manifests as an overshoot at higher temperatures (304 and 301 K) but an "undershoot" at lower temperatures (295 and 292 K), with essentially no overshoot at the intermediate temperature of 298 K. We do not currently have an explanation for the existence of two distinct intensification phases with separate temperature dependencies, but it is an important topic for future work.

The dependence of the intensification rate on SST is dramatically larger than that predicted by E12 theory based on PI. Indeed, V_p varies only by 26% between the coldest and warmest simulations (46 vs. 58 m s^{-1}), which translates to a relatively modest change in the normalized intensification rates predicted by E12 theory. This qualitative result does not change if one were to define V_p internally in the model based on, for example, a high-percentile value of V from each simulation. Doing so does widen the range of values of V_p (not shown) but still falls well short of explaining the range of intensification rates. Moreover, this internal definition yields a wider range in V_p solely because of the overshooting at warmer temperatures (Figure 15). This outcome suggests that an internally defined V_p likely ought to avoid the transient overshoot period following initial rapid intensification, in which case it will again yield a relatively small range of values.

We may go one step further and test the extent to which variations in the fluid depth h may explain this discrepancy. For this to be possible, based on the intrinsic time scale in Equation 5, h must decrease with increasing V_p (or SST) in order to amplify the effect of varying V_p alone. We hypothesize that there are two plausible options for relevant variations in h: (1) the tropospheric depth and (2) the boundary layer depth. The former, however, will increase with warming (Figure 1a) (e.g., Cronin & Chavas, 2019; Khairoutdinov & Emanuel, 2013) and would thus act in the wrong direction. In contrast, the latter is expected to decrease with warming; in the cold/dry limit, the boundary layer depth effectively extends through the depth of the troposphere (Cronin & Chavas, 2019).

Multiple methods exist for defining the top of the boundary layer, including using the bulk Richardson number (Ri_b) (e.g., Hanna, 1969; Mahrt, 1981), the lifted condensation level (LCL) (e.g., Hansen & Back, 2015), and the depth of the convective mixed layer (i.e., a layer of nearly constant θ or θ_v; Stull, 1988). When applied to the TC boundary layer in particular, these candidate definitions result in a wide spread in h (Zhang et al., 2011), and Kepert et al. (2016) demonstrated that the TC boundary layer is quite distinct from the traditional conceptual model of a "well-mixed" layer due to substantial diabatic effects. Here, h, like V_p, is calculated from the 5-day mean state immediately prior to TC seed time, and we estimate it using three methods: (i) a critical Ri_b of 0.125, (ii) the LCL, and (iii) the top of the mixed layer, defined here as the height at which θ_v matches its value at the lowest model level (e.g., Seidel et al., 2010).

Table 1 shows boundary layer depth values using each of these methods. All three methods indeed show boundary layer depth decreasing with increasing SST. The Bulk Richardson number method yields the largest fractional variation, and thus we use this range of values to test the inclusion of variable h in Equation 5. Specifically, since $h = 5{,}000$ m yields a good fit to the warmest simulation (304 K), we retain $h = 5{,}000$ m at 304 K and then rescale h in proportion to changes in h_{BL} from Table 1. The result with varying h is also

Table 1
Mean Boundary Layer Depth (h [m]) Versus SST (K) Using Three Different Calculation Methods: Bulk Richardson, LCL, and Mixed Layer Depth

SST	h_{bulkRI}	h_{LCL}	h_{ML}
292	1,508	747	751
295	1,374	710	750
298	1,361	701	745
301	1,372	690	744
304	1,267	642	672

Note. See text for details. Values are calculated from a 5-day mean state immediately prior to seed time, then averaged over the ensemble at a given SST.

shown in Figure 15 for the 292 K case (dotted line), which exhibits the largest fractional change in h_{BL} (+19%). This modification only modestly reduces the discrepancy between simulations and theory.

Thus, we conclude that the theoretical prediction of E12, though admirable in its elegance and analytic simplicity, is likely missing some important unknown physical processes, perhaps whose temperature dependence is independent of PI. It is worth emphasizing the direction of this error: Emanuel (2017) used E12 theory to argue that intensification rates are likely to increase under global warming (thus reducing lead times for impact forecasting) owing to the increase in PI; our idealized simulations suggest that intensification rates may increase significantly more rapidly with warming than E12 theory predicts.

5. Discussion and Summary

The sensitivity of the time to spontaneous TC genesis and maximum intensification rate to climate warming over a broad range of SSTs has been investigated in this work, expanding on the findings of Nolan et al. (2007) and similar subsequent studies (e.g., Davis, 2015; Muller & Romps, 2018; Nolan & Rappin, 2008; Rappin et al., 2010; Wing et al., 2016). The evolution to spontaneous TC genesis from the RCE state can be broken down into two stages: (i) the time from the initial undisturbed state to a precursor seed disturbance and (ii) the time between the seed disturbance and genesis, referred to as the incubation period. Spontaneous seed development and subsequent tropical cyclogenesis occur in all of our 25 simulations across the full range of SSTs tested (292 to 304 K), even in the absence of radiative feedbacks. The time to seed exhibits a strong nonmonotonic "U" shape response to surface warming and associated changes in the background state (Figure 1), with the shortest ensemble-mean time to seed ($\mu = 28.6$ days) occurring at the middle SST of 298 K. At 292 and 304 K, the seed times are considerably longer ($\mu = 47.1$ days and $\mu = 59.5$ days, respectively) with individual ensemble members falling outside the range of the 298 K ensemble, despite moderate internal variability.

In an attempt to explain this nonmonotonicity, we examined changes in thermodynamic parameters, taken from the RCE background state, that are empirically related to TC genesis in the real world: namely, PI V_p, midtropospheric relative humidity RH, and saturation deficit χ. In the current setup, V_p increases more or less linearly with warming (Figure 5) and therefore is not well correlated with changes in the seed times. RH and χ also increase monotonically with warming and so cannot independently explain the "U" shape dependence of the seed times on SST. The relatively fast path to seed development at 298 K is possibly due to the combination of V_p and χ, assuming favorable environments for seeds share some similarities with genesis (increasing V_p should favor cyclogenesis, whereas increasing χ should limit it; therefore, an optimal thermodynamic state is likely at the intermediate value of SST).

We evaluated two commonly used GPIs, GPI-EN04 and GPI-E10, to see if these may help explain the response of the explicitly simulated seed rates to warming. However, neither GPI-EN04 nor GPI-E10 was able to reproduce the nonmonotonic "U" shape of seed times in Figure 5. That said, it is not clear that GPIs apply directly to the idealized simulations here because they are derived based on multiple observed storms that form from incipient vortices, whereas our simulated TCs evolve from a base state of rest. Nevertheless, GPI-EN04 increases substantially as SST increases from 292 to 304 K, owing to positive trends in both V_p and RH. This result is qualitatively consistent with multimodel mean projections of GPI-EN04 in CMIP5 models (Camargo, 2013). GPI-E10, on the other hand, exhibits a much flatter response to warming due to the compensating influences of V_p and χ (e.g., Camargo et al., 2014).

Ultimately, we do know what sets the long time scale to a seed disturbance. We speculate that a tendency toward organized convective structures due to enhanced convective gustiness (e.g., cold pools) in the early stages of simulation may be playing a role (e.g., Davis, 2015; Smith & Nicholls, 2019; Wang et al., 2019). Such structures are apparent within the first 5 to 15 days in the 292 and 295 K simulations (Figure 3). On the other hand, the convection in the 304 K simulations is relatively homogeneous and unchanged from its initial state during this period (Figures 3d and 3e). It is plausible that increased convective turbulence

within the boundary layer acts as an expedient for convective self-aggregation that is not accounted for in commonly used diagnostics (e.g., Muller & Romps, 2018; Wing et al., 2016; Wing & Emanuel, 2014). Indeed, Yang (2018) has suggested that the boundary layer plays a fundamental role in the onset of nonrotating self-aggregation (in particular, diabatic processes that contribute to the production of APE). A detailed analysis of the role of boundary-layer processes in simulations of rotating self-aggregation is left for future work.

The incubation period of a TC shows less systematic dependence on SST compared to the longer seed gestation periods, although there is a tendency toward longer and more variable incubation times at the highest SSTs of 301 and 304 K, ranging between 1 and 13 days. The increased stochasticity of incubation times at these higher SSTs may be driven in part by physical differences of the seeds themselves at the onset of incubation. A seed is defined here based on a threshold (−4 hPa) anomaly of smoothed minimum surface pressure. At this threshold, the incipient disturbances manifest typically as broad, cold-core vortices, with a maximum circulation between 3 and 5 km and radius of maximum winds ranging between 150 and 300 km (Figure 4), but there is inherent variability in these structures between different ensemble members.

An analysis of the relationship between incubation period and GPI-relevant thermodynamic factors for a given SST (Figure 8) indicates that shorter incubation periods are most often associated with larger values of PI V_p (e.g., Nolan et al., 2007), smaller values of saturation deficit χ (e.g., Rappin et al., 2010), and higher values of midlevel RH. When these variables are combined to form three commonly used GPIs—GPI-EN04, GPI-E10, and Λ^{-1}—the relationship with incubation period is as one might expect: Incipient vortices develop more rapidly into TCs when embedded in high GPI environments, and vice-versa (Figure 9). The 304 K ensemble appears to be an outlier in terms of its interensemble scatter relationship with GPI. In an assessment of the relationship between ensemble-mean GPI and the inverse of the incubation period, both GPI-EN04 and GPI-E10 track the explicitly simulated genesis rates reasonably well up to 301 K. Between 301 and 304 K, the GPI trends diverge owing to the humidity variables used in their formulation, with the χ-dependent GPI-E10 decreasing like the simulated incubation behavior and the RH-dependent GPI-EN04 increasing even further. This diverging behavior resembles the "two diverging genesis scenarios" recently shown by Lee et al. (2020) in their assessment of GPIs and future synthetic track frequencies in GCMs. Our results suggest that the saturation deficit may be the more relevant humidity variable for assessing future trends in TC frequency.

It should be pointed out that the vertical shear term in all three GPIs is neglected, consistent with the imposed initial states, and although some vertical shear inevitably develops as convection evolves, it is found to be very small (<2 m s^{-1} below the tropopause). Despite its absence here, the presence of deep-layer shear is unquestionably an important factor for discriminating between developing and nondeveloping convective systems, as has been shown both observationally (e.g., DeMaria et al., 2001; Gray, 1979; McBride & Zehr, 1981) and in idealized models similar to the present study (e.g., Nolan & Rappin, 2008; Rappin et al., 2010).

Lower-tropospheric (2–6 km) RH variability was assessed to see if it may help explain the onset of spontaneous seeds or cyclogenesis in our simulations. At the time of genesis, the RH within the core is substantially higher than the domain-mean for all SSTs, whereas the RH anomaly in the core at the time of a seed disturbance is somewhat lower. Therefore, the evolution of lower-tropospheric humidity variability in the domain appears to be an important precursor to TC genesis, consistent with previous studies on spontaneous cyclogenesis in rotating RCE (Muller & Romps, 2018; Wing et al., 2016). The development of a seed, however, may be less determined by lower-tropospheric moisture anomalies. An example was found in our simulations of a seed disturbance developing in the absence of positive moisture anomalies. Further research is needed to understand the salient mechanisms controlling the onset of weak, precursor TC disturbances in rotating RCE.

Finally, the response of the maximum intensification rate ($\Delta V_{\max}$) of TCs to surface warming has been investigated. Unlike the incubation period, $\Delta V_{\max}$ increases monotonically with warming at a rate that scales more or less linearly with the increase in V_p. This suggests that TC intensification rates are likely to increase, or continue to increase (e.g., Bhatia et al., 2019), in a warmer climate due to a larger surface moisture disequilibrium, consistent with recent results from GCM projections (e.g., Bhatia et al., 2018;

Emanuel, 2017; Emanuel, 2020). The dependence of intensification rate on SST obtained from the idealized simulations here is dramatically larger than that predicted by the intensification theory of Emanuel (2012) based on variations in PI (Figure 15), suggesting that this theory, though elegant in its simplicity, may be missing some important unknown physical processes. An alternative, ventilation-based intensification theory produces a very similar prediction as the Emanuel (2012) theory, though its time scale is arbitrary. The very strong dependence of intensification rate on SST is specific to the second half of the intensification process and is reminiscent of the "overshoot" period identified in past studies. Why intensification appears to behave so differently in the early versus late stages of rapid intensification is currently unknown. Overall, the large increase in simulated intensification rates with warming suggests that the challenges for operational forecasting in a future, warmer climate (e.g., reduced lead times for impact forecasting) could be even greater than expectations from theoretical predictions.

Appendix A: Sensitivity to Radiation Scheme

A second set of small-domain simulations was carried out but with an interactive radiation scheme (Rapid Radiative Transfer Model (RRTM); Mlawer et al., 1997) to assess what impact the simple fixed radiative cooling scheme (Equation 1) might have on the characteristics of the RCE states and the resulting GPIs. These additional simulations were performed on a 96 × 96 km domain with 2 km horizontal grid spacing to prevent self-aggregation. The standard 392 × 392 km with 4 km grid spacing at 298 K resulted in a cluster of convection forming as an elongated line at first and then transitioning to a circular region after about 75 days, similar to Wing and Emanuel (2014). The solar insolation is fixed 409.6 W m^{-2} (i.e., no diurnal cycle, corresponding to a 0–20° tropical annual-mean solar constant of 515.58 W m^{-2} and a zenith angle of 42.05°; Wing et al., 2018). The surface albedo is set to 0.07. In terms of GPI-relevant variables, the main difference between the RCE states with interactive radiation and fixed tropospheric cooling manifests in the midtropospheric RH, with 600-hPa RH varying by about 4% across SSTs with interactive radiation (71% at 292 K to 75% at 304 K) compared to 14% variation using the fixed cooling scheme (61% at 292 K to 75% at 304 K). Consequently, relative-humidity dependent GPIs, such as EN04, depend less sensitively on SST in our setup when using interactive radiation.

Data Availability Statement

CM1 output data and input files are available through the CSIRO Data Access Portal (https://doi.org/10.25919/5f7138a8a8c37).

Acknowledgments

We are grateful to Kevin Walsh, Allison Wing, Kerry Emanuel, George Bryan, and Marcus Thatcher for stimulating discussions on the topic. We thank David Nolan, Brian Tang, and Stephen Garner for their thorough and insightful reviews of earlier versions of the manuscript. HAR acknowledges support from the Australian Research Council Discovery Project (DP150102272) as well as the Australian National Environmental Science Programme (NESP). This research was undertaken with the assistance of resources from the National Computational Infrastructure (NCI Australia), an NCRIS enabled capability supported by the Australian Government. We also thank George Bryan for providing and maintaining the CM1 model. M. S. acknowledges support from the Australian Research Council through DECRA award DE190100866. D. R. C. acknowledges support from National Science Foundation Grant 10001413.

References

Alland, J. J., Tang, B. H., & Corbosiero, K. L. (2017). Effects of midlevel dry air on development of the axisymmetric tropical cyclone secondary circulation. *Journal of the Atmospheric Sciences*, *74*(5), 1455–1470.

Balaguru, K., Foltz, G. R., & Leung, L. R. (2018). Increasing magnitude of hurricane rapid intensification in the central and eastern tropical Atlantic. *Geophysical Research Letters*, *45*, 4238–4247. https://doi.org/10.1029/2018GL077597

Bhatia, K., Vecchi, G., Murakami, H., Underwood, S., & Kossin, J. (2018). Projected response of tropical cyclone intensity and intensification in a global climate model. *Journal of Climate*, *31*(20), 8281–8303. https://doi.org/10.1175/JCLI-D-17-0898.1

Bhatia, K. T., Vecchi, G. A., Knutson, T. R., Murakami, H., Kossin, J., Dixon, K. W., & Whitlock, C. E. (2019). Recent increases in tropical cyclone intensification rates. *Nature Communications*, *10*(1), 1–9. https://doi.org/10.1038/s41467-019-08471-z

Bister, M., & Emanuel, K. A. (1997). The genesis of Hurricane Guillermo: TEXMEX analyses and a modeling study. *Monthly Weather Review*, *125*, 2662–2682. https://doi.org/10.1175/1520-0493(1997)125h2662:tgohgti2.0.co;2

Bister, M., & Emanuel, K. A. (2002). Low frequency variability of tropical cyclone potential intensity 1. Interannual to interdecadal variability. *Journal of Geophysical Research*, *107*(D24), 4801. https://doi.org/10.1029/2001JD000776

Braun, S. A., Sippel, J. A., & Nolan, D. S. (2012). The impact of dry midlevel air on hurricane intensity in idealized simulations with no mean flow. *Journal of the Atmospheric Sciences*, *69*(1), 236–257. https://doi.org/10.1175/JAS-D-10-05007.1

Bretherton, C. S., Blossey, P. N., & Khairoutdinov, M. (2005). An energy-balance analysis of deep convective self-aggregation above uniform SST. *Journal of the Atmospheric Sciences*, *62*(12), 4273–4292. https://doi.org/10.1175/JAS3614.1

Brown, B. R., & Hakim, G. J. (2013). Variability and predictability of a three-dimensional hurricane in statistical equilibrium. *Journal of the Atmospheric Sciences*, *70*(6), 1806–1820. https://doi.org/10.1175/JAS-D-12-0112.1

Bruyère, C. L., Holland, G. J., & Towler, E. (2012). Investigating the use of a genesis potential index for tropical cyclones in the North Atlantic Basin. *Journal of Climate*, *25*(24), 8611–8626. https://doi.org/10.1175/JCLI-D-11-00619.1

Bryan, G. H. (2003). An investigation of the convective region of numerically simulated squall lines (PhD thesis). The Pennsylvania State University.

Bryan, G. H. (2012). Effects of surface exchange coefficients and turbulence length scales on the intensity and structure of numerically simulated hurricanes. *Monthly Weather Review*, *140*(4), 1125–1143. https://doi.org/10.1175/MWR-D-11-00231.1

Bryan, G. H., & Fritsch, J. M. (2002). A benchmark simulation for moist nonhydrostatic numerical models. *Monthly Weather Review*, *130*(12), 2917–2928. https://doi.org/10.1175/1520-0493(2002)130%3C2917:ABSFMN%3E2.0.CO;2

Bryan, G. H., & Rotunno, R. (2009). The maximum intensity of tropical cyclones in axisymmetric numerical model simulations. *Monthly Weather Review*, *137*(6), 1770–1789. https://doi.org/10.1175/2008MWR2709.1

Camargo, S. J. (2013). Global and regional aspects of tropical cyclone activity in the CMIP5 models. *Journal of Climate*, *26*(24), 9880–9902. https://doi.org/10.1175/JCLI-D-12-00549.1

Camargo, S. J., Emanuel, K. A., & Sobel, A. H. (2007). Use of a genesis potential index to diagnose ENSO effects on tropical cyclone genesis. *Journal of Climate*, *20*(19), 4819–4834. https://doi.org/10.1175/JCLI4282.1

Camargo, S. J., Tippett, M. K., Sobel, A. H., Vecchi, G. A., & Zhao, M. (2014). Testing the performance of tropical cyclone genesis indices in future climates using the HiRAM model. *Journal of Climate*, *27*(24), 9171–9196. https://doi.org/10.1175/JCLI-D-13-00505.1

Carrasco, C. A., Landsea, C. W., & Lin, Y. L. (2014). The influence of tropical cyclone size on its intensification. *Weather and Forecasting*, *29*(3), 582–590. https://doi.org/10.1175/WAF-D-13-00092.1

Carstens, J. D., & Wing, A. A. (2020). Tropical cyclogenesis from self-aggregated convection in numerical simulations of rotating radiative-convective equilibrium. *Journal of Advances in Modeling Earth Systems*, *12*, e2019MS002020. https://doi.org/10.1029/2019MS002020

Chavas, D. R. (2013). Tropical cyclone size in observations and in radiative-convective equilibrium (PhD thesis). Massachusetts Institute of Technology.

Chavas, D. R. (2017). A simple derivation of tropical cyclone ventilation theory and its application to capped surface entropy fluxes. *Journal of the Atmospheric Sciences*, *74*(9), 2989–2996. https://doi.org/10.1175/JAS-D-17-0061.1

Chavas, D. R., & Emanuel, K. (2014). Equilibrium tropical cyclone size in an idealized state of axisymmetric radiative-convective equilibrium. *Journal of the Atmospheric Sciences*, *71*(5), 1663–1680. https://doi.org/10.1175/JAS-D-13-0155.1

Chavas, D. R., & Reed, K. A. (2019). Dynamical aquaplanet experiments with uniform thermal forcing: System dynamics and implications for tropical cyclone genesis and size. *Journal of the Atmospheric Sciences*, *76*(8), 2257–2274.

Christensen, J. H., Krishna Kumar, K., Aldrian, E., An, S.-I., Cavalcanti, I. F. A., de Castro, M., et al. (2013). Climate phenomena and their relevance for future regional climate change. In T. F. Stocker, et al. (Eds.), *Climate change 2013: The physical science basis. Contribution of Working Group I to the Fifth Assessment Report of the Intergovernmental Panel on Climate Change* (Chap. 14, pp. 1217–1308). Cambridge, UK and New York, NY: Cambridge University Press. https://doi.org/10.1017/CBO9781107415324.028

Cione, J. J. (2015). The relative roles of the ocean and atmosphere as revealed by buoy air-sea observations in hurricanes. *Monthly Weather Review*, *143*(3), 904–913. https://doi.org/10.1175/MWR-D-13-00380.1

Črnivec, N., Smith, R. K., & Kilroy, G. (2016). Dependence of tropical cyclone intensification rate on sea-surface temperature. *Quarterly Journal of the Royal Meteorological Society*, *142*(697), 1618–1627. https://doi.org/10.1002/qj.2752

Cronin, T. W., & Chavas, D. R. (2019). Dry and semidry tropical cyclones. *Journal of the Atmospheric Sciences*, *76*(8), 2193–2212. https://doi.org/10.1175/JAS-D-18-0357.1

Dare, R. A., & McBride, J. L. (2011). The threshold sea surface temperature condition for tropical cyclogenesis. *Journal of Climate*, *24*(17), 4570–4576. https://doi.org/10.1175/JCLI-D-10-05006.1

Davis, C. A. (2015). The formation of moist vortices and tropical cyclones in idealized simulations. *Journal of the Atmospheric Sciences*, *72*(9), 3499–3516. https://doi.org/10.1175/JAS-D-15-0027.1

Defforge, C. L., & Merlis, T. M. (2017). Evaluating the evidence of a global sea surface temperature threshold for tropical cyclone genesis. *Journal of Climate*, *30*(22), 9133–9145. https://doi.org/10.1175/JCLI-D-16-0737.1

DeMaria, M., Knaff, J. A., & Connell, B. H. (2001). A tropical cyclone genesis parameter for the tropical Atlantic. *Weather and Forecasting*, *16*(2), 219–233. https://doi.org/10.1175/1520-0434(2001)016%3C0219:ATCGPF%3E2.0.CO;2

Donelan, M. A., Haus, B. K., Reul, N., Plant, W. J., Stiassnie, M., Graber, H. C., et al. (2004). On the limiting aerodynamic roughness of the ocean in very strong winds. *Geophysical Research Letters*, *31*, L18306. https://doi.org/10.1029/2004GL019460

Drennan, W. M., Zhang, J. A., French, J. R., McCormick, C., & Black, P. G. (2007). Turbulent fluxes in the hurricane boundary layer. *Part II: Latent Heat Flux Journal Atmosphere Science*, *64*, 1103–1115. https://doi.org/10.1175/JAS3889.1

Emanuel, K. (2006). Climate and tropical cyclone activity: A new model downscaling approach. *Journal of Climate*, *19*(19), 4797–4802. https://doi.org/10.1175/JCLI3908.1

Emanuel, K. (2010). Tropical cyclone activity downscaled from NOAA-CIRES reanalysis, 1908–1958. *Journal of Advances in Modeling Earth Systems*, *2*, 1. https://doi.org/10.3894/JAMES.2010.2.1

Emanuel, K. (2012). Self-stratification of tropical cyclone outflow. Part II: Implications for storm intensification. *Journal of the Atmospheric Sciences*, *69*(3), 988–996. https://doi.org/10.1175/JAS-D-11-0177.1

Emanuel, K. (2017). Will global warming make hurricane forecasting more difficult? *Bulletin of the American Meteorological Society*, *98*(3), 495–501. https://doi.org/10.1175/BAMS-D-16-0134.1

Emanuel, K. (2020). Response of global tropical cyclone activity to increasing CO_2: Results from downscaling CMIP6 models. *Journal of Climate*. https://doi.org/10.1175/JCLI-D-20-0367.1

Emanuel, K., & Nolan, D. S. (2004). Tropical cyclone activity and the global climate system. In *26th Conference on Hurricanes and Tropical Meteorology* (pp. 240–241).

Emanuel, K., Solomon, S., & Folini, D. (2013). Influence of tropopause transition layer cooling on Atlantic hurricane activity. *Journal of Climate*, *26*, 2288–2301.

Emanuel, K., Sundararajan, R., & Williams, J. (2008). Hurricanes and global warming: Results from downscaling IPCC AR4 simulations. *Bulletin of the American Meteorological Society*, *89*(3), 347–368. https://doi.org/10.1175/BAMS-89-3-347

Emanuel, K. A. (1995). Sensitivity of tropical cyclones to surface exchange coefficients and a revised steady-state model incorporating eye dynamics. *Journal of the Atmospheric Sciences*, *52*(22), 3969–3976. https://doi.org/10.1175/1520-0469(1995)052%3C3969:SOTCTS%3E2.0.CO;2

Emanuel, K. A. (2013). Downscaling CMIP5 climate models shows increased tropical cyclone activity over the 21st century. *Proceedings of the National Academy of Sciences*, *110*(30), 12,219–12,224. https://doi.org/10.1073/pnas.1301293110

Fairall, C. W., Bradley, E. F., Hare, J. E., Grachev, A. A., & Edson, J. B. (2003). Bulk parameterization of air-sea fluxes: Updates and verification for the COARE algorithm. *Journal of Climate*, *16*(4), 571–591. https://doi.org/10.1175/1520-0442(2003)016%3C0571:BPOASF%3E2.0.CO;2

Frank, W. M., & Young, G. S. (2007). The interannual variability of tropical cyclones. *Monthly Weather Review.*, *135*(10), 3587–3598. https://doi.org/10.1175/MWR3435.1

Gray, W. M. (1968). Global view of the origin of tropical disturbances and storms. *Monthly Weather Review*, *96*(10), 669–700.

Gray, W. M. (1979). Hurricanes: Their formation, structure and likely role in the tropical circulation. In D. B. Shaw (Ed.), *Meteorology Over the Tropical Oceans* (pp. 155–218). Grenville Place, Bracknell: James Glaisher House.

Hakim, G. J. (2011). The mean state of axisymmetric hurricanes in statistical equilibrium. *Journal of the Atmospheric Sciences*, *68*(6), 1364–1376. https://doi.org/10.1175/2010JAS3644.1

Hanna, S. R. (1969). The thickness of the planetary boundary layer. *Atmospheric Environment (1967)*, *3*(5), 519–536. https://doi.org/10.1016/0004-6981(69)90042-0

Hansen, Z. R., & Back, L. E. (2015). Higher surface Bowen ratios ineffective at increasing updraft intensity. *Geophysical Research Letters*, *42*, 10,503–10,511. https://doi.org/10.1002/2015GL066878

Held, I. M., & Zhao, M. (2008). Horizontally homogeneous rotating radiative-convective equilibria at GCM resolution. *Journal of the Atmospheric Sciences*, *65*(6), 2003–2013. https://doi.org/10.1175/2007JAS2604.1

Hoogewind, K. A., Chavas, D. R., Schenkel, B. A., & O'Neill, M. E. (2020). Exploring controls on tropical cyclone count through the geography of environmental favorability. *Journal of Climate*, *33*(5), 1725–1745. https://doi.org/10.1175/JCLI-D-18-0862.1

Johnson, N. C., & Xie, S. P. (2010). Changes in the sea surface temperature threshold for tropical convection. *Nature Geoscience*, *3*, 842–845. https://doi.org/10.1038/ngeo1008

Kang, N.-Y., & Elsner, J. B. (2019). Influence of global warming on the rapid intensification of western North Pacific tropical cyclones. *Environmental Research Letters*, *14*(4), 44027. https://doi.org/10.1088/1748-9326/ab0b50

Kepert, J. D., Schwendike, J., & Ramsay, H. (2016). Why is the tropical cyclone boundary layer not well mixed? *Journal of the Atmospheric Sciences*, *73*(3), 957–973. https://doi.org/10.1175/JAS-D-15-0216.1

Khairoutdinov, M., & Emanuel, K. (2013). Rotating radiative-convective equilibrium simulated by a cloud-resolving model. *Journal of Advances in Modeling Earth Systems*, *5*, 816–825. https://doi.org/10.1002/2013MS000253

Kilroy, G., & Smith, R. K. (2015). Tropical cyclone convection: The effects of a vortex boundary-layer wind profile on deep convection. *Quarterly Journal of the Royal Meteorological Society*, *141*(688), 714–726. https://doi.org/10.1002/qj.2383

Knutson, T., Camargo, S. J., Chan, J. C. L., Emanuel, K., Ho, C.-H., Kossin, J., et al. (2020). Tropical cyclones and climate change assessment: Part II. Projected response to anthropogenic warming. *Bulletin of the American Meteorological Society*, *101*(0), E303–E322. https://doi.org/10.1175/BAMS-D-18-0194.1

Knutson, T. R., McBride, J. L., Chan, J., Emanuel, K., Holland, G., Landsea, C., et al. (2010). Tropical cyclones and climate change. *Nature Geoscience*, *3*, 157–163. https://doi.org/10.1038/ngeo779

Korty, R. L., Camargo, S. J., & Galewsky, J. (2012). Tropical cyclone genesis factors in simulations of the Last Glacial Maximum. *Journal of Climate*, *25*(12), 4348–4365. https://doi.org/10.1175/JCLI-D-11-00517.1

Korty, R. L., Emanuel, K. A., Huber, M., & Zamora, R. A. (2017). Tropical cyclones downscaled from simulations with very high carbon dioxide levels. *Journal of Climate*, *30*(2), 649–667. https://doi.org/10.1175/JCLI-D-16-0256.1

Kowch, R., & Emanuel, K. (2015). Are special processes at work in the rapid intensification of tropical cyclones? *Monthly Weather Review*, *143*(3), 878–882.

Lander, M. A., & Guard, C. P. (1998). A look at global tropical cyclone activity during 1995: Contrasting high Atlantic activity with low activity in other basins. *Monthly Weather Review*, *126*(5), 1163–1173. https://doi.org/10.1175/1520-0493(1998)126%3C1163:ALAGTC%3E2.0.CO;2

Lee, C., Camargo, S. J., Sobel, A. H., & Tippett, M. K. (2020). Statistical-dynamical downscaling projections of tropical cyclone activity in a warming climate: Two diverging genesis scenarios. *Journal of Climate*, *33*, 4815–4834. https://doi.org/10.1175/JCLI-D-19-0452.1

Lee, C.-Y., Tippett, M. K., Sobel, A. H., & Camargo, S. J. (2018). An environmentally forced tropical cyclone hazard model. *Journal of Advances in Modeling Earth Systems*, *10*, 223–241. https://doi.org/10.1002/2017MS001186

Mahrt, L. (1981). Modelling the depth of the stable boundary-layer. *Boundary-Layer Meteorology*, *21*(1), 3–19. https://doi.org/10.1007/BF00119363

Mallard, M. S., Lackmann, G. M., & Aiyyer, A. (2013). Atlantic hurricanes and climate change. Part II: Role of thermodynamic changes in decreased hurricane frequency. *Journal of Climate*, *26*(21), 8513–8528. https://doi.org/10.1175/JCLI-D-12-00183.1

Maue, R. N. (2011). Recent historically low global tropical cyclone activity. *Geophysical Research Letters*, *38*, L14803. https://doi.org/10.1029/2011GL047711

McBride, J. L., & Zehr, R. (1981). Observational analysis of tropical cyclone formation. Part II: Comparison of non-developing versus developing systems. *Journal of the Atmospheric Sciences*, *38*(6), 1132–1151. https://doi.org/10.1175/1520-0469(1981)038%3C1132:OAOTCF%3E2.0.CO;2

McGauley, M. G., & Nolan, D. S. (2011). Measuring environmental favorability for tropical cyclogenesis by statistical analysis of threshold parameters. *Journal of Climate*, *24*, 5968–5997. https://doi.org/10.1175/2011JCLI4176.1

Menkes, C. E., Lengaigne, M., Marchesiello, P., Jourdain, N. C., Vincent, E. M., Lefèvre, J., et al. (2012). Comparison of tropical cyclogenesis indices on seasonal to interannual timescales. *Climate Dynamics*, *38*(1), 301–321. https://doi.org/10.1007/s00382-011-1126-x

Merlis, T. M., & Held, I. M. (2019). Aquaplanet simulations of tropical cyclones. *Current Climate Change Reports*, *5*(3), 185–195. https://doi.org/10.1007/s40641-019-00133-y

Merlis, T. M., Zhou, W., Held, I. M., & Zhao, M. (2016). Surface temperature dependence of tropical cyclone-permitting simulations in a spherical model with uniform thermal forcing. *Geophysical Research Letters*, *43*, 2859–2865. https://doi.org/10.1002/2016GL067730

Mlawer, E. J., Taubman, S. J., Brown, P. D., Iacono, M. J., & Clough, S. A. (1997). Radiative transfer for inhomogeneous atmospheres: RRTM, a validated correlated-k model for the longwave. *Journal of Geophysical Research*, *102*(D14), 16,663–16,682. https://doi.org/10.1029/97JD00237

Morrison, H., Curry, J. A., & Khvorostyanov, V. I. (2005). A new double-moment microphysics parameterization for application in cloud and climate models. Part I: Description. *Journal of the Atmospheric Sciences*, *62*(6), 1665–1677. https://doi.org/10.1175/JAS3446.1

Morrison, H., Thompson, G., & Tatarskii, V. (2009). Impact of cloud microphysics on the development of trailing stratiform precipitation in a simulated squall line: Comparison of one- and two-moment schemes. *Monthly Weather Review*, *137*(3), 991–1007. https://doi.org/10.1175/2008MWR2556.1

Muller, C. J., & Romps, D. M. (2018). Acceleration of tropical cyclogenesis by self-aggregation feedbacks. *Proceedings of the National Academy of Sciences*, *115*(12), 2930–2935. https://doi.org/10.1073/pnas.1719967115

Nolan, D. S. (2007). What is the trigger for tropical cyclogenesis? *Australian Meteorological Magazine*, *56*(4), 241–266.

Nolan, D. S., & Rappin, E. D. (2008). Increased sensitivity of tropical cyclogenesis to wind shear in higher SST environments. *Geophysical Research Letters*, *35*, L14805. https://doi.org/10.1029/2008GL034147

Nolan, D. S., Rappin, E. D., & Emanuel, K. A. (2007). Tropical cyclogenesis sensitivity to environmental parameters in radiative-convective equilibrium. *Quarterly Journal of the Royal Meteorological Society*, *133*(629), 2085–2107. https://doi.org/10.1002/qj.170

Palmen, E. H. (1948). On the formation and structure of tropical cyclones. *Geophysica*, *3*, 26–38.

Ramsay, H. (2017). The global climatology of tropical cyclones. In *Oxford Research Encyclopedia of Natural Hazard Science*. New York: Oxford University Press. https://doi.org/10.1093/acrefore/9780199389407.013.79

Ramsay, H. A. (2013). The effects of imposed stratospheric cooling on the maximum intensity of tropical cyclones in axisymmetric radiative-convective equilibrium. *Journal of Climate*, *26*(24), 9977–9985. https://doi.org/10.1175/JCLI-D-13-00195.1

Rappin, E. D., Nolan, D. S., & Emanuel, K. A. (2010). Thermodynamic control of tropical cyclogenesis in environments of radiative-convective equilibrium with shear. *Quarterly Journal of the Royal Meteorological Society*, *136*(653), 1954–1971. https://doi.org/10.1002/qj.706

Raymond, D. J., Sessions, S. L., & Lopez Carrillo, C. (2011). Thermodynamics of tropical cyclogenesis in the northwest Pacific. *Journal of Geophysical Research*, *116*, D18101. https://doi.org/10.1029/2011JD015624

Riemer, M., & Laliberté, F. (2015). Secondary circulation of tropical cyclones in vertical wind shear: Lagrangian diagnostic and pathways of environmental interaction. *Journal of the Atmospheric Sciences*, *72*(9), 3517–3536.

Ritchie, E. A., & Holland, G. J. (1997). Scale interactions during the formation of Typhoon Irving. *Monthly Weather Review*, *125*, 1377–1396. https://doi.org/10.1175/1520-0493(1997)125h1377:sidtfoi2.0.co;2

Royer, J.-F., Chauvin, F., Timbal, B., Araspin, P., & Grimal, D. (1998). A Gcm study of the impact of greenhouse gas increase on the frequency of occurrence of tropical cyclones. *Climatic Change*, *38*(3), 307–343. https://doi.org/10.1023/A:1005386312622

Schreck, C. J., Knapp, K. R., & Kossin, J. P. (2014). The impact of best track discrepancies on global tropical cyclone climatologies using IBTrACS. *Monthly Weather Review*, *142*(10), 3881–3899. https://doi.org/10.1175/MWR-D-14-00021.1

Seidel, D. J., Ao, C. O., & Li, K. (2010). Estimating climatological planetary boundary layer heights from radiosonde observations: Comparison of methods and uncertainty analysis. *Journal of Geophysical Research*, *115*, D16113. https://doi.org/10.1029/2009JD013680

Smith, W. P., & Nicholls, M. E. (2019). On the creation and evolution of small-scale low-level vorticity anomalies during tropical cyclogenesis. *Journal of the Atmospheric Sciences*, *76*, 2335–2355. https://doi.org/10.1175/JAS-D-18-0104.1

Sobel, A. H., Camargo, S. J., Hall, T. M., Lee, C.-Y., Tippett, M. K., & Wing, A. A. (2016). Human influence on tropical cyclone intensity. *Science*, *353*(6296), 242–246. https://doi.org/10.1126/science.aaf6574

Stull, R. B. (1988). *An introduction to boundary layer meteorology*. Dordrecht, Netherlands: Springer. Retrieved from https://books.google.com.au/books?id=eRRz9RNvNOkC

Sugi, M., Yamada, Y., Yoshida, K., Mizuta, R., Nakano, M., Kodama, C., & Satoh, M. (2020). Future changes in the global frequency of tropical cyclone seeds. *SOLA*, *16*. https://doi.org/10.2151/sola.2020-012

Tang, B., & Camargo, S. J. (2014). Environmental control of tropical cyclones in CMIP5: A ventilation perspective. *Journal of Advances in Modeling Earth Systems*, *6*, 115–128. https://doi.org/10.1002/2013MS000294

Tang, B., & Emanuel, K. (2010). Midlevel ventilation's constraint on tropical cyclone intensity. *Journal of the Atmospheric Sciences*, *67*(6), 1817–1830. https://doi.org/10.1175/2010JAS3318.1

Tang, B., & Emanuel, K. (2012). A ventilation index for tropical cyclones. *Bulletin of the American Meteorological Society*, *93*(12), 1901–1912. https://doi.org/10.1175/BAMS-D-11-00165.1

Tang, B. H., Rios-Berrios, R., Alland, J. J., Berman, J. D., & Corbosiero, K. L. (2016). Sensitivity of axisymmetric tropical cyclone spinup time to dry air aloft. *Journal of the Atmospheric Sciences*, *73*, 4269–4287. https://doi.org/10.1175/JAS-D-16-0068.1

Tippett, M. K., Camargo, S. J., & Sobel, A. H. (2011). A Poisson regression index for tropical cyclone genesis and the role of large-scale vorticity in genesis. *Journal of Climate*, *24*(9), 2335–2357. https://doi.org/10.1175/2010JCLI3811.1

Tory, K. J., & Dare, R. A. (2015). Sea surface temperature thresholds for tropical cyclone formation. *Journal of Climate*, *28*(20), 8171–8183. https://doi.org/10.1175/JCLI-D-14-00637.1

Tory, K. J., Ye, H., & Dare, R. A. (2018). Understanding the geographic distribution of tropical cyclone formation for applications in climate models. *Climate Dynamics*, *50*(7–8), 2489–2512. https://doi.org/10.1007/s00382-017-3752-4

Vecchi, G. A., Delworth, T. L., Murakami, H., Underwood, S. D., Wittenberg, A. T., Zeng, F., et al. (2019). Tropical cyclone sensitivities to CO_2 doubling: Roles of atmospheric resolution, synoptic variability and background climate changes. *Climate Dynamics*, *53*(9-10), 5999–6033. https://doi.org/10.1007/s00382-019-04913-y

Vecchi, G. A., Fueglistaler, S., Held, I. M., Knutson, T. R., & Zhao, M. (2013). Impacts of atmospheric temperature trends on tropical cyclone activity. *Journal of Climate*, *26*, 3877–3891. https://doi.org/10.1175/JCLI-D-12-00503.1

Walsh, K. J. E., Mcbride, J. L., Klotzbach, P. J., Balachandran, S., Camargo, S. J., Holland, G., et al. (2016). Tropical cyclones and climate change. *Wiley Interdisciplinary Reviews: Climate Change*, *7*(1), 65–89. https://doi.org/10.1002/wcc.371

Wang, S., Camargo, S. J., Sobel, A. H., & Polvani, L. M. (2014). Impact of the tropopause temperature on the intensity of tropical cyclones—An idealized study using a mesoscale model. *Journal of the Atmospheric Sciences*, *71*, 4333–4348. https://doi.org/10.1175/JAS-D-14-0029.1

Wang, Y., Davis, C. A., & Huang, Y. (2019). Dynamics of lower-tropospheric vorticity in idealized simulations of tropical cyclone formation. *Journal of the Atmospheric Sciences*, *76*(3), 707–727. https://doi.org/10.1175/JAS-D-18-0219.1

Wing, A. A., Camargo, S. J., & Sobel, A. H. (2016). Role of radiative-convective feedbacks in spontaneous tropical cyclogenesis in idealized numerical simulations. *Journal of the Atmospheric Sciences*, *73*(7), 2633–2642. https://doi.org/10.1175/JAS-D-15-0380.1

Wing, A. A., & Emanuel, K. A. (2014). Physical mechanisms controlling self-aggregation of convection in idealized numerical modeling simulations. *Journal of Advances in Modeling Earth Systems*, *6*, 59–74. https://doi.org/10.1002/2013MS000269

Wing, A. A., Reed, K. A., Satoh, M., Stevens, B., Bony, S., & Ohno, T. (2018). Radiative-convective equilibrium model intercomparison project. *Geoscientific Model Development*, *11*, 793–813.

Yang, D. (2018). Boundary layer diabatic processes, the virtual effect, and convective self-aggregation. *Journal of Advances in Modeling Earth Systems*, *10*, 2163–2176. https://doi.org/10.1029/2017MS001261

Zhang, J. A., & Montgomery, M. T. (2012). Observational estimates of the horizontal eddy diffusivity and mixing length in the low-level region of intense hurricanes. *Journal of the Atmospheric Sciences*, *69*, 1306–1316. https://doi.org/10.1175/JAS-D-11-0180.1

Zhang, J. A., Rogers, R. F., Nolan, D. S., & Marks, F. D. (2011). On the characteristic height scales of the hurricane boundary layer. *Monthly Weather Review*, *139*(8), 2523–2535. https://doi.org/10.1175/MWR-D-10-05017.1